MG ZONATION AND HETEROGENEITY IN LOW-MG CALCITE MICROCRYSTALS OF A DEPOSITIONAL CHALK

CHANSE J. RINDERKNECHT,[1,2] FRANEK J. HASIUK,[1] AND STEPHAN C. OBORNY[1]

[1]*Kansas Geological Survey, University of Kansas, 1930 Constant Avenue, Lawrence, Kansas 66047, U.S.A.*
[2]*Department of Geology, University of Kansas, 1414 Naismith Drive, Lawrence Kansas, 66045, U.S.A.*

ABSTRACT: **Diagenetic low-magnesium calcite (LMC) microcrystals constitute the framework that hosts most micropores in limestone reservoirs and therefore create the storage capacity for hydrocarbons, water, and anthropogenic CO_2. Limestones dominated by LMC microcrystals are also commonly used for paleoclimate reconstructions and chemostratigraphic correlations. LMC microcrystals are well known to exhibit a range of textures (e.g., granular, fitted, clustered), but there exists uncertainty with regard to how these textures form. One hypothesis is that during crystal growth, Mg is incorporated into diagenetic overgrowths (cement), where the chemical zonation and microtexture may reflect diagenetic processes. To evaluate small-scale geochemical zonation in LMC microcrystals, this study uses scanning electron microscopy (SEM) and energy-dispersive spectroscopy (EDS) to measure the Mg/Ca ratio across the interiors of LMC granular microcrystals from a Late Cretaceous marine chalk from the Tor Fm. (Norwegian North Sea).**

Mg/Ca zonation was identified in all LMC microcrystals with a diameter > 5 μm. Generally, the cores of large crystals have lower Mg/Ca (≈ 5.9 mmol/mol) and the rims have elevated Mg/Ca (≈ 13 mmol/mol). Smaller microcrystals (< 5 μm) show no resolvable zonation, but do exhibit a wide range in Mg/Ca content from 2.9 to 32.2 mmol/mol. Measured Mg/Ca values are arbitrarily divided into three populations: low Mg (average ≈ 5.9 mmol/mol), intermediate Mg (average ≈ 13.3 mmol/mol), and high Mg (average ≈ 20 mmol/mol). The observed zonation and Mg enrichment within LMC microcrystals is interpreted to reflect depositional as well as multiple diagenetic signals, such as constructive precipitation through recrystallization and pore-filling cementation.

Although chalk from the Tor Fm. is dominated by granular euhedral LMC microcrystals, using SEM-EDS to find Mg/Ca heterogeneity in other LMC microcrystal textures may provide insight into the diagenetic processes that create textural variations in micropore-dominated limestones. The Mg data also more broadly suggest that there is useful, measurable diagenetic information in material that is otherwise considered homogeneous. Distinguishing between possible primary compositions and secondary cementation has implications for studies that rely on the primary chemistry of fine-grained carbonate deposits (e.g., micrite), such as paleoclimatology, Mg paleothermometry, and chemostratigraphy.

INTRODUCTION

Effective reservoir characterization requires quantifying porosity and permeability. Regardless of reservoir fluid (e.g., hydrocarbon, water, or anthropogenic CO_2), these petrophysical attributes represent storage capacity and connectivity and can be classified as either micropore or macropore systems depending on pore size and shape (Lucia 2007). Microporosity in a reservoir can constitute a significant part of overall storage capacity (Leverett 1941; Lucia 2007), yet the diminutive size of the pore throats connecting these micropores results in much lower fluid flow rates (Rezaee and Kazemzadeh 2006). In giant hydrocarbon reservoirs, a significant part of oil-in-place can be hosted in micropores because column height is large enough to overcome their entry pressure (Lucia 2007). In fields with smaller column heights, micropores often remain uncharged. The resulting high-water saturation accompanied by high porosity-log readings yields a phenomenon known as "low-resistivity pay" (Pittman 1971; Cantrell and Haggerty 1999; Maliva et al. 2009; Vincent et al. 2011).

Micropore-dominated reservoirs ($> 80\%$ of pore volume) can exhibit exceedingly low residual oil saturations (Fullmer et al. 2014).

Models to explain micropore systems are continuously emerging (e.g., Scholle 1977; Budd 1989; Moshier 1989; Fabricius 2007; Volery et al. 2010a, 2010b; Deville de Periere et al. 2011; Lucia 2017). Micropores can be observed in a wide array of carbonate facies and in nearly every constituent of a limestone, including carbonate matrix, skeletal, and nonskeletal allochems (Kaczmarek et al. 2015). Some workers have found that syndepositional characteristics have little effect on pore geometry or pore-throat size distribution and that micropores, and associated pore and pore-throat geometries, are often the result of postdepositional alteration (Budd 1989; Moshier 1989; Deville de Periere et al. 2011; Lucia and Loucks 2013; Loucks et al. 2013). The pervasive occurrence of micropores suggests that their development is fundamental in the diagenetic process (Kaczmarek et al. 2015), though the formational processes are still debated (Hashim and Kaczmarek 2019). It is suggested that micropores are created

either through destructive dissolution, during which micropores develop in an otherwise nonporous hostrock (Oldershaw 1972; Jameson 1994), or that micropores remain as pore space is occluded during constructive precipitation (Folk 1965; Loucks et al. 2013; Hasiuk et al. 2016). Most research supports the constructive model and suggests that the process occurs during shallow burial (Moshier 1989; Loucks et al. 2013; Kaczmarek et al. 2015; Hasiuk et al. 2016; Lucia 2017). Research shows that most micropores are hosted among low-magnesium calcite (LMC) microcrystals (Moshier 1989; Budd 1989; Kaczmarek et al. 2015). Therefore, the diagenetic evolution of LMC microcrystals is considered to have a direct effect on porosity and permeability in limestone reservoirs.

Ninety percent of LMC microcrystal texture observed in limestones can be assigned to one of three textural classes, each containing two subclasses (Kaczmarek et al. 2015). These textures are *granular* (*subhedral* or *euhedral*), *clustered* (*loose* or *fused*), and *fitted* (*partial* or *fused*). Each descriptive class has a characteristic porosity, permeability, and pore-throat size distribution, thereby providing a predictive relationship between microcrystalline textures and reservoir properties (Kaczmarek et al. 2015). Though this classification is useful, it does not imply a genetic origin for the microcrystalline framework. Therefore, a knowledge gap exists between the genetic relationship of various textures of LMC microcrystals and the specific diagenetic environments or physiochemical processes involved in their formation and evolution.

Previous research illustrates that many LMC microcrystals grow as precipitated cement in existing pore space (Kaczmarek et al. 2015; Hasiuk et al. 2016). As a result, LMC microcrystals could be hypothesized to have distinct primary sediment and subsequent cement chemical signatures like coarser calcite cements (e.g., Meyers and Lohmann 1985; Heydari and Moore 1993). Thus, knowing whether LMC microcrystals are chemically zoned would be an important step toward better understanding LMC microcrystal origin and the diagenetic processes that contribute to their evolution. However, analysis of chemical zonation in LMC microcrystals using cathodoluminescence, secondary ion mass spectrometry, and electron microprobe analyses has proven difficult because of the resolution required to analyze crystals that have a modal diameter of $\approx$ 2 µm (Kaczmarek et al. 2015). Recently, field-emission scanning electron microscopes (SEM) and energy-dispersive spectroscopy (EDS) using silicon drift detectors (SDD) have become advanced enough to allow sub-µm scale chemical signatures to be detected. Therefore, the goal of this study is to apply these newer analytical approaches to investigate Mg zonation in LMC microcrystals. Through these data, we aim to gain a better understanding about the origin of LMC microcrystals and their genetic relationship between microcrystal texture and the physiochemical processes and environments where these microcrystals form.

To test this approach, a depositional chalk composed of calcite microcrystals was chosen because the primary mineralogy is simpler (LMC) and the subsequent diagenetic pathway (burial in a relatively closed hydrologic system, Schlanger and Douglas 1974; Scholle 1977) is more straightforward than shallow-marine limestones that typically start with a mixed, metastable mineral composition (Friedman 1964; Bathurst 1975) and may have experienced a more complex diagenetic history given the proximity of the depositional system to a fluctuating sea level. Chalk diagenesis also serves as a good proxy for better understanding LMC carbonate rocks, such as those hypothesized to be deposited during "calcite seas" or in lacustrine environments (e.g., Sandberg 1983; Ries 2010; Hashim and Kaczmarek 2019).

GEOLOGIC BACKGROUND

Geological Setting

The Tor Formation (Cretaceous, late Campanian to Maastrichtian) is a coccolith-dominated microporous limestone deposited in the North Sea (Fig. 1). Previous studies have documented the presence of granular euhedral, clustered-loose, and fitted-partial microcrystalline textures in the Tor Formation (Kaczmarek et al. 2015), making it an ideal candidate for analysis in this study. The core samples examined come from well 16/2-1, which was drilled in 1967 (Norwegian Petroleum Directorate 16/2-1).

The North Sea Central Graben, where the well is located, is a result of Late Jurassic extensional rifting that began near the end of the Callovian and persisted until the Berriasian (Møller and Rasmussen 2003). Following Jurassic rifting, there was a period of post-rift subsidence, which was subsequently modified by halokinetic salt movement in the Late Cretaceous (Vejbæk and Andersen 2002). The post-rift subsidence was followed by uplift along pre-existing extensional faults as a result of compression (Jakobsen and Andersen 2010). The compression created topographic highs and local depocenters, where sea-level rise accommodated thick successions of strata in the depocenters (Jakobsen and Andersen 2010; Back et al. 2011; Van Buchem et al. 2018; Van Der Voet et al. 2019). The coccolith-dominated Tor Formation consists of debris flows and slump features generated as a result of the dynamic tectonic environment (Back et al. 2011; Smit et al. 2018).

Chalk Diagenesis and Evolution

Chalks have been studied extensively via scientific ocean drilling programs and by the petroleum industry (e.g., in the North Sea). The diagenetic evolution and subsequent petrologic features found in chalks are dictated by the primary sediment mineralogy, sediment size, deposition rate, and temperature (Schlanger and Douglas 1974; Scholle 1977; Grützner and Mienert 1999; Fabricius 2003, 2007). With this, chalk diagenesis is dominated by five processes: mechanical compaction, recrystallization, development of contact cements, chemical compaction, and pore-filling cementation (Schlanger and Douglas 1974; Fabricius 2007).

At the time of deposition, ooze has nearly 70% porosity and most of the sediment retains its primary characteristics (i.e., recognizable coccospheres, articulated coccoliths, disaggregated coccolith plates, and foraminifera). At burial depths between 70 and 300 m below the sea floor (mbsf), the sediment undergoes mechanical compaction, resulting in a decline in primary porosity to $\approx$ 50% (Schlanger and Douglas 1974; Scholle 1977; Borre and Fabricius 1998; Fabricius 2007). During mechanical compaction, the sedimentary particles maintain primary particle morphology and size (Schlanger and Douglas 1974; Grützner and Mienert 1999).

With deeper burial, recrystallization and contact cementation begin, which continues to alter depositional characteristics of coccolith debris and can significantly decrease porosity (Fabricius 2007). The rate of recrystallization depends on organic content, pore-fluid chemistry, temperature, and rate of burial (Borre and Fabricius 1998; Fabricius 2007; Lakshtanov et al. 2018). During this stage of diagenesis, the LMC-dominated sediments undergo a recrystallization process that progressively coarsens the primary sediment and is often responsible for the loss of primary characteristics in the sedimentary particles (Hashim and Kaczmarek 2019). Contact cementation, which is the precipitation of cements at grain-to-grain contacts often between larger grains and recrystallized sediments, can be concurrent and is often caused by recrystallization (Fabricius 2003). Such recrystallization is evidenced in the North Sea chalks by smooth edges on fossil debris, coarsening of crystals, and the euhedral nature of the LMC microcrystals (Fabricius 2007). Some of the pelagic fossil material can still be distinguished, but recrystallization has significantly altered most of the material. If recrystallization continues (e.g., due to a slow mechanical compaction rate), contact cementation may progress until crystals touch (Schlanger and Douglas 1974; Fabricius 2007).
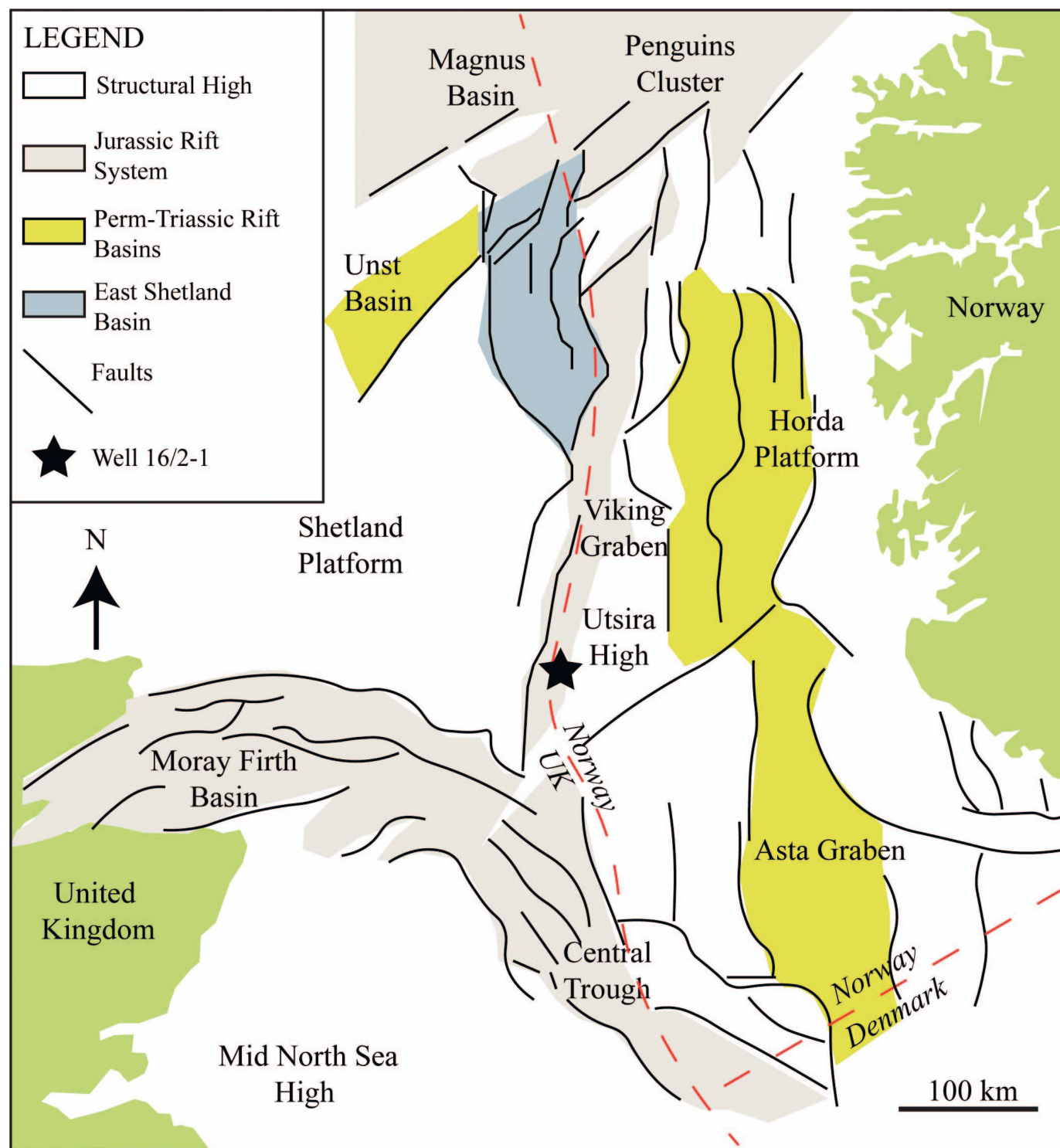
Fig. 1.—Simplified structural map of the North Sea, modified after Niazi et al. (2019). Well 16/2-1 is located in the southwestern part of the Norwegian North Sea on the eastern part of the Utsira High. Extensional faulting during the Jurassic and Cretaceous, and related subsidence, created the accommodation for deposition of the Tor Fm chalk.

Chemical compaction, or the dissolution and compaction of carbonate material, occurs as chalks undergo further burial. Stylolitization is a common feature associated with this late-stage diagenetic event, and petrographic studies have attributed extensive stylolitization during chemical compaction to clay abundance in the chalk (Lind 1993). Stylolitization and the dissolution of calcite at the calcite–clay interface is the source of calcite for the last stage of diagenesis, pore-filling cementation (Fabricius 2007). The $\delta^{18}O$ of pore-filling calcite cement has

been shown to generally be the same as the primary sediments, suggesting a closed geochemical system in which late cements and recrystallized matrix are in isotopic equilibrium (Jørgensen 1987).

METHODS

Twenty core plugs from well 16/2-1 between depths 5708 and 5834 ft (1740–1779 m) were chosen for this study. Each of the 20 core plugs was used to collect porosity and isotopic data through helium pyncnometry and mass spectrometry, respectively. Four of the core plugs—Tor1 (5,708.7 ft, 1,740 m), Tor2 (5,711.3 ft, 1,740.8 m), Tor20 (5,790.5 ft, 1,765.9 m), and Tor38 (5,834.6 ft, 1778.4 m)—were analyzed via SEM-EDS. Tor1 (shallowest) and Tor38 (deepest) were selected to assess the effect of depth. The presence of stylolites and routine core analysis data indicated that Tor2 and Tor20 represent low-porosity zones and were therefore assumed to represent zones of increased microcrystal cementation.

Scanning Electron Microscopy

Highly spatially resolved scanning electron microscopy (SEM) and electron-dispersive spectroscopy (EDS) elemental data were collected at two separate analytical facilities. Equipment included an FEI Quanta 250 field-emission scanning electron microscope (FE-SEM) coupled with an Oxford X-Max[n] EDS detector at the Materials Analysis Research Laboratory (Iowa State University, Ames, Iowa, USA) and an FEI Teneo FE-SEM coupled with an Oxford X-Max[n] EDS detector at the Sensitive Instrument Facility (Ames Laboratory, U.S. Department of Energy, Ames, Iowa, USA). Work was initiated on the Quanta, but instrument breakdown required long-term maintenance, leading to the use of the Teneo. Both instruments have equal capabilities and employed the same silicon drift detector (SDD). The Oxford X-Max[n] EDS SDD has an area of 80 mm[2] for detection of emitted X-rays. The area of the SDD is critical because larger SDD allow increased count rates at lower beam currents and lower accelerating voltages. Therefore, a larger detector enables the analysis of more X-rays ultimately improving X-ray detection (Collins et al. 2009).

To obtain SEM images of freshly broken surfaces and analyze texture and morphology, approximately 10 g of chalk from the core plugs were mounted on metal conductive plates using carbon glue. The samples were subsequently evacuated overnight to ensure complete outgassing of the pore system. These surfaces were then analyzed using backscatter electron (BSE) and secondary electron (SE) techniques. SE and BSE imaging were conducted with an acceleration voltage of 10 kV and working distance of 10–14.4 mm. The four samples analyzed for geochemical zonation were embedded in an epoxy resin and polished using a 0.25 μm pad. Epoxy-impregnated samples were carbon-coated and reimaged using BSE imaging from 50× to 5,000× magnification. An accelerating voltage of 8 kV was used to minimize interaction volume in the sample while still providing enough energy to emit the Ca X-ray, an element critical for the identification of geochemical zonation.

Energy-Dispersive Spectroscopy and Interaction Volume

Casino Software (Drouin et al. 2007) was used to model EDS interaction volumes in calcite via Monte Carlo electron trajectory simulations (Fig. 2) under various accelerating voltages. Interaction volume dictates spatial resolution (Goldstein et al. 2017; see Fig. 2), meaning the location and spatial area where X-rays will be emitted and measured during EDS analysis. The larger the interaction volume, the lower the spatial resolution. Interaction volume is a function of the atomic number of the material, the accelerating voltage, and the angle at which the electron beam strikes the sample surface (Goldstein et al. 2017). Lower-atomic-number elements allow deeper penetration of the electron beam because there are fewer protons with which to interact, resulting in less elastic scattering (Fig. 3).

As accelerating voltage increases, interaction volume also increases. However, accelerating voltage must overcome the excitation energy needed to generate the statistically significant X-rays from the target element. In short, higher accelerating voltages result in deeper penetration into the sample and allow higher-atomic-number elements to be detected.

Previous work suggests that to acquire measurable X-rays in calcite, the ratio of beam energy to ionization energy (i.e., overvoltage ratio) must be at least two X-rays (Goldstein et al. 2017). To measure Mn and Fe, accelerating voltages of 12 kV and 15 kV, respectively, are required to provide enough energy in the primary beam to overcome the critical ionization energy to obtain a statistically significant amount of Mn and Fe K-alpha X-rays (Goldstein et al. 2017; see Fig 3). This accelerating voltage would increase the interaction volume in the carbonate sample and provide a spatial resolution of $\approx$ 3.5 μm[3] according to our Monte Carlo simulations (Fig 2). However, when small crystals (1–3 μm in diameter) are analyzed under such conditions, any apparent zonation may be an artifact of X-rays being collected from surrounding microcrystals. Using 8 kV provided an interaction volume of only $\approx$ 0.5 μm[3] according to our Monte Carlo simulations (Fig. 2) thus high-enough spatial resolution for detection of zonation in lower-mass elements like Mg and Ca in small crystals.

Fourteen Tor 1, seven Tor2, eight Tor20, and eight Tor38 LMC microcrystals were analyzed in each of the four Tor core plug samples. At each site, microcrystals from 2 to 10 μm in diameter were imaged and analyzed via EDS. Line scans were conducted to obtain a qualitative data set on spatial variation of Mg/Ca in a calcite microcrystal at the sub-μm scale. Each line scan was performed across the diameter of the crystal $\approx$ 100 times to maximize the signal-to-noise ratio. To obtain chemical compositions along the otherwise qualitative line scans, spot analyses (spot size $\approx$ 5 nm) were performed at the core and rim of each microcrystal ($\approx$ 10-minute count time per spot). Spot analyses provided the quantitative atomic fraction of each element in the crystal, which was then converted into a millimoles per mole magnesium-to-calcium ratio (mmol/mol Mg/ Ca). Spectra were collected and quantified using both the ZAF (atomic number, self-absorption effect, and fluorescence effect) and phi-rho-Z (ionization distribution plotted against mass depth) methods using the Oxford software and showed little difference between the two methods (Goldstein et al. 1992). Oxide percentage of each EDS spot analyzed in this study was > 98%. The qualitative line scans and quantitative point analyses provided a balance between quantitative data (points) and understanding the spatial variation of the elemental ratios in the microcrystals (line scans). Thirty-nine qualitative line scans and 75 quantitative point analyses were conducted.

Crystal Size Distribution and Characterization of Crystal Morphology

SEM images from the polished Tor1, Tor2, Tor20, and Tor38 samples were used to obtain crystal size distribution (CSD). In each sample, the long axes of 300 crystals were measured to the nearest 0.1 μm at 1500× using ImageJ. All SEM images of calcite–calcite and clay–calcite interfaces were analyzed for evidence of dissolution such as dissolution layers, dissolution pits, or dissolution ledges (Hashim and Kaczmarek 2021). The overall morphology of LMC microcrystals was also characterized using the methodology of Kaczmarek et al. (2015).

Helium Pycnometry

The 20 Tor core plugs were measured for bulk effective porosity via helium pycnometry (American Petroleum Institute 1998). This process consists of three measurements: mass, bulk volume, and grain volume. Mass was measured using a Mettler Toledo ME204D analytical balance (analytical precision $\pm$ 0.1 mg). Bulk volume was calculated using dimensions measured to the nearest 0.01 mm with digital calipers (Mitutoyo Absolute Aos Digimatic calipers). Grain volume was calculated
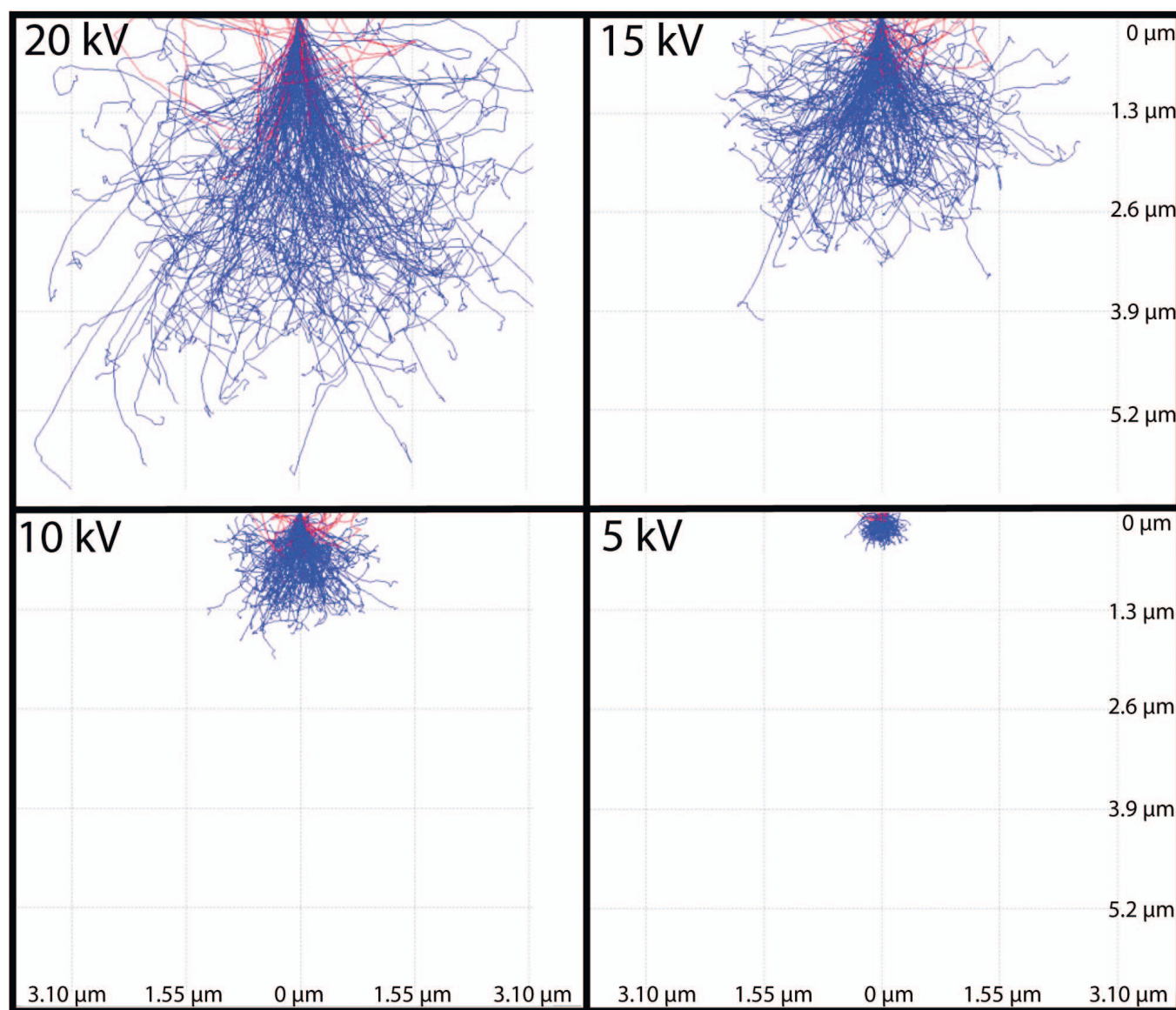
F<small>IG</small>. 2.—Examples of X-ray and sample interaction volumes in calcite as a function of accelerating voltages of 20 kV to 5 kV. Red lines represent backscattered electrons, and blue represent secondary electrons. Lines derived from Monte Carlo simulations with Casino software (Drouin et al. 2007).

using Boyle's Law (Boyle 1662) on a Micromeritics AccuPyc II 1340 helium pycnometer. Each core plug was fully filled and vented with helium gas for 10 cycles before measurements of grain volume were recorded.

Stable-Isotope Analyses

Approximately 1 mg of powdered bulk sample was collected for stable carbon and oxygen isotopic analysis from each of the 20 Tor core plugs. Isotope ratios were measured on a Finnigan MAT Delta Plus XL mass spectrometer in continuous-flow mode connected to a gas bench with a CombiPAL autosampler (Stable Isotope Paleo Environments Research Group, Iowa State University, Ames, Iowa, USA). Reference standards (NBS-18, NBS-19) were used for isotopic corrections and to assign the data to the appropriate isotopic scale. Corrections were done using a regression method, and isotope results are reported in parts per thousand (per mil, ‰) deviation from the VPDB standard. Analytical uncertainty for $\delta^{13}C$ is ± 0.02‰ (VPDB) and for $\delta^{18}O$ is ± 0.09‰ (VPDB).

RESULTS

SEM Imaging and Crystal Size Distribution

Kaczmarek et al. (2015) defined "microporosity" or a "micropore system" based on the sizes and texture of the LMC microcrystal framework hosting micropores. Tor Formation samples studied by Kaczmarek et al. (2015) were shown to include three distinct textures: granular-euhedral, clustered-loose, and fitted-partial. The crystal morphology found throughout the Tor samples analyzed in this study, regardless of depth, was dominantly granular-euhedral (Fig. 4). This texture is defined as a loose framework of randomly oriented, well-formed (euhedral) rhombic microcrystals. This texture also exhibits distinct microcrystals, curvilinear or straight crystal edges, and relatively short crystal interfaces.

The 3D, broken-surface SE and BSE images also provide a more accurate and detailed representation of rock texture than 2D images alone. Although many individual coccoliths are distinguishable, they are
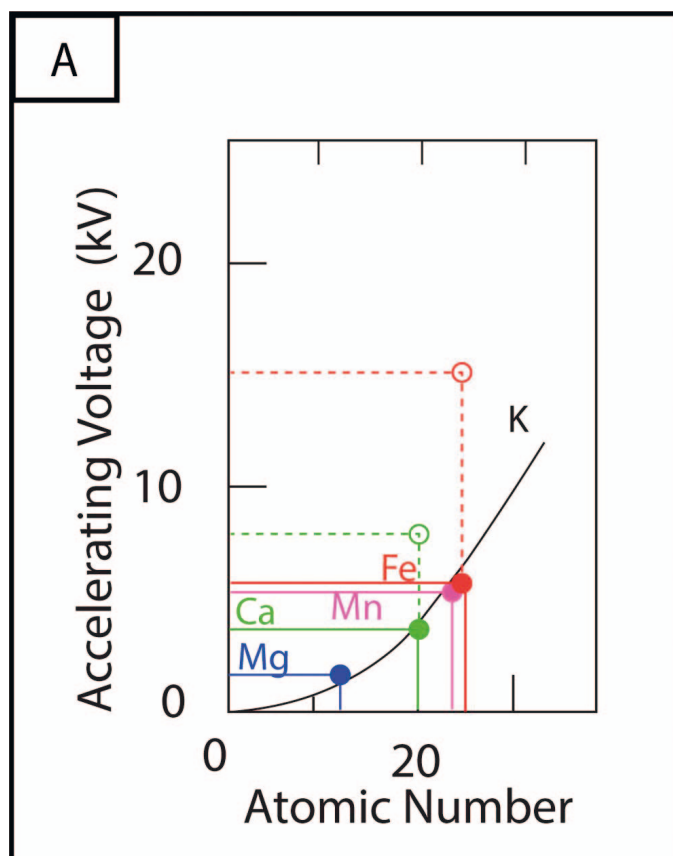
6.9 mmol/mol. Newly acquired geochemical data indicate core-to-rim Mg/Ca zonation in large microcrystals and variable Mg enrichment in many small microcrystals (Figs. 6–9; Table 1).

In general, large microcrystals exhibited zonation with lower Mg/Ca in the cores (average 5.6 mmol/mol) and higher Mg/Ca in the rims (average 16 mmol/mol). Large microcrystal cores ranged in diameter from 1.9 to 3.7 μm, with rim thickness measuring 2.9–5.0 μm. Two of three large microcrystals in Tor1 (Fig. 6; Table 1) exhibit low, 2.9–3.6 mmol/mol Mg/Ca at the core and higher Mg/Ca in the rim (12.3–25.2 mmol/mol). A third particularly large microcrystal (8 μm) has Mg/Ca of 15 mmol/mol at the core and 6.5 mmol/mol at the rim. The largest microcrystal in sample Tor2 (Fig. 7) is 5.0 μm in diameter, with a 2.1-μm-diameter core (0.7 mmol/mol) and 2.9-μm-thick rim (14.2 mmol/mol). In sample Tor20 (Fig. 8), no large microcrystals were analyzed because of LMC microcrystal aggradation and scarcity. In sample Tor38 (Fig. 9), the largest microcrystal is 6.9 μm, with a 1.9-μm-diameter core (5.7 mmol/mol) and 5-μm-thick rim (22.2 mmol/mol).

Thirty-two-line scans and 60 points were measured in small crystals. These microcrystals tend to have elevated Mg/Ca, averaging 14.1 mmol/mol (range of 3.5–32.2 mmol/mol). The average value is similar to the Mg/Ca measured in the rims of larger microcrystals.

Collectively, the Mg/Ca results define three distinct calcite populations in the Tor Formation (Fig. 10). Population 1 is characterized by very low Mg/Ca (< 8 mmol/mol) with an average of 5.6 mmol/mol. These Mg/Ca values occur in the cores of four of the large microcrystals, the rim of one large microcrystal, and nine of the small microcrystals. Population 2 is characterized by intermediate Mg/Ca (10–15 mmol/mol) with an average of 13.3 mmol/mol. Intermediate Mg/Ca values were detected on the rims of two of the larger crystals, the core of one large crystal, and 14 of the small microcrystals. Population 3 is characterized by elevated Mg/Ca (> 17.8 mmol/mol) with an average of 23.3 mmol/mol and is found on the rim of two large crystals and nine of the small microcrystals.

Helium Porosimetry

The helium porosity of core plugs ranged from 15.1% to 20.6% (Fig. 11A), with an average of 18% ± 1.5% (1σ). A high porosity zone of ≈ 20% is present between 5,727 ft and 5,748 ft (1,746 and 1,752 m, respectively), a zone associated with a high density of dissolution seams and fractures. Reported porosities in the Tor Formation are as high as 40% (Van den Bark and Thomas 1981; Dunn 1975), but these high values were not measured here.

STABLE-ISOTOPE ANALYSES

Bulk measurements of stable isotopes range between –8.1 and –6.3‰ $\delta^{18}O$ and +1.9 and +2.4‰ $\delta^{13}C$ with no clear trends with depth (Fig. 11B, C). Previous work has shown that Late Cretaceous and Paleogene chalks range from ≈ –9 to –2‰ $\delta^{18}O$ and ≈ –2 to +5‰ $\delta^{13}C$ (see summary Fig. 5 of Hasiuk et al. 2016), with a clearer correlation between increasing depth and more negative $\delta^{18}O$ (Scholle 1977; Fabricius 2003, 2007).

DISCUSSION

Zonation has been shown in macro-calcite cements (Meyers and Lohmann 1985; Heydari and Moore 1993) and in large dolomite crystals (Ryan et al. 2019) but to our knowledge, this is the first time Mg zonation and heterogeneity have been documented in diagenetic calcite microcrystals. While not discounting dissolution as a mechanism for altering calcite microcrystal texture (Hashim and Kaczmarek 2021), the observed zonation and heterogeneity is strong evidence of constructive cementation in the Tor chalk, but the observed Mg/Ca variations across the LMC microcrystals

Fig. 3.—Relation between scanning-electron-microscopy accelerating voltage and detection of various elements in calcite. Accelerating voltage must overcome the critical ionization energy of an element by a factor of two (termed the "overvoltage") to obtain statistically significant X-ray counts. The solid black line represents the critical ionization energy to obtain Kα X-rays. Solid colored lines represent the critical ionization energy of common carbonate trace elements. Dotted lines illustrate overvoltage for Ca (green) and Fe (red). High-atomic-number elements require higher accelerating voltages to meet the overvoltage.

generally disarticulated and have overgrowths (Fig. 4). Clay particles are generally rare although somewhat more abundant in Tor20.

The CSD of Tor LMC microcrystals was previously characterized by an average of "slightly more than 2 μm" (Kaczmarek et al. 2015). The mean diameter of microcrystals as analyzed in this study was 2.9 μm (Tor1, Tor2, Tor20, and Tor38) with a range of 0.5–10 μm (Fig. 5). However, the LMC microcrystals proved to be divided into two classes based on presence of Mg/Ca zonation. LMC microcrystals lacking zonation had diameters less than 5 μm and were classified as "small." The mean diameter of these microcrystals was 2.4 μm (range, 1.1–3.9 μm). LMC microcrystals showing Mg/Ca zonation had diameters greater than 5 μm and were classified as "large." These large microcrystals have a mean diameter of 6.6 μm (range, 5–8 μm). The SEM images and CSD clearly indicate the Tor Formation is dominated by small microcrystals (Figs. 4, 5), yet larger crystals do exist. The calculations of Kaczmarek et al. (2015) were performed on freshly broken surfaces (three-dimensional surfaces) at 5000×, CSDs were calculated in this study from polished samples two-dimensional surfaces at 1500×.

SEM-EDS

Bulk Mg/Ca ratios measured via inductively coupled plasma mass spectrometry (ICP-MS) were reported in Hasiuk et al. (2016) to average
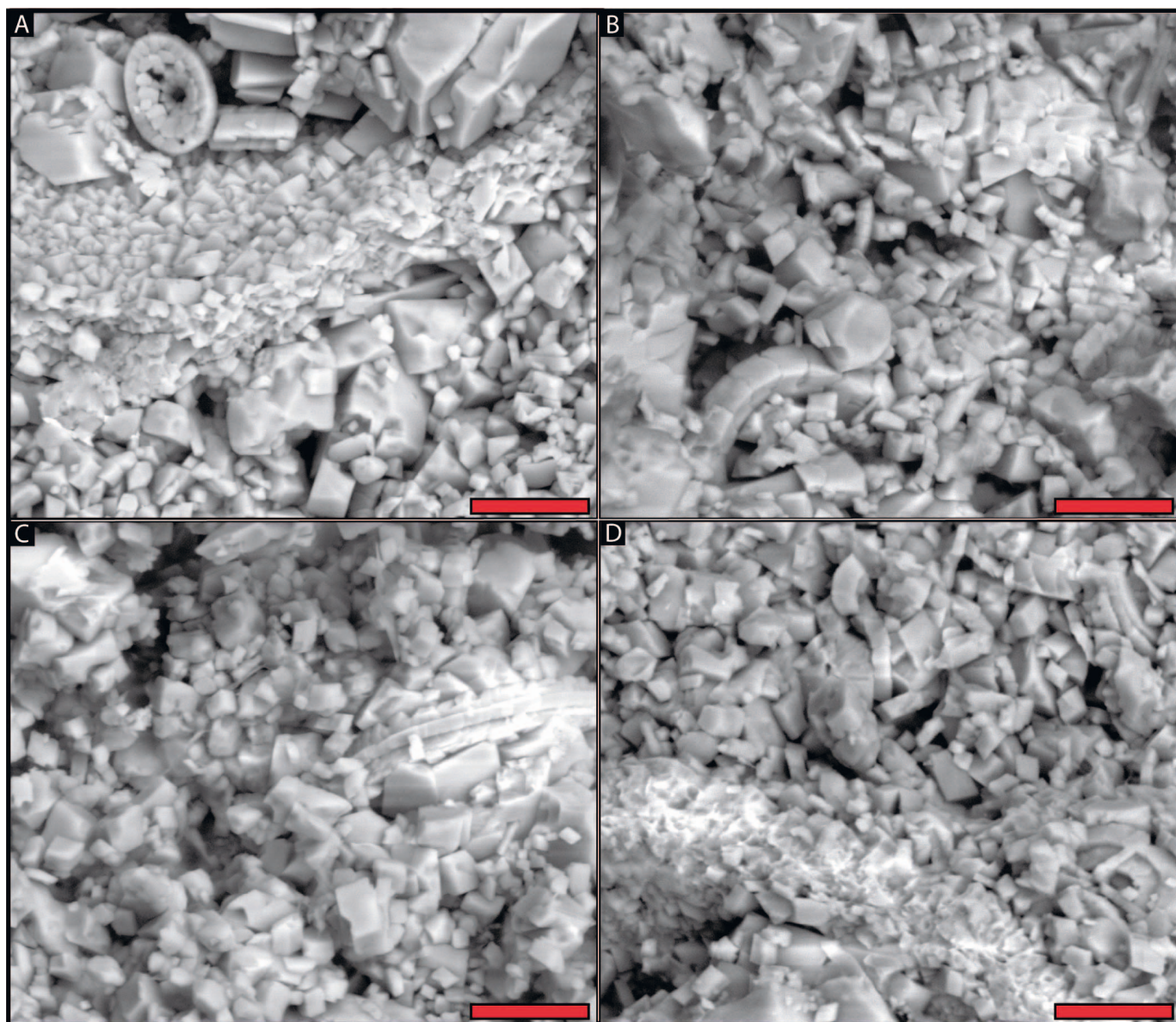
Fig. 4.—Backscatter electron images of microcrystals in the Tor Formation. Letters A, B, C, and D correspond with Tor1, Tor2, Tor20, and Tor 38, and therefore represent increasing depth, respectively, through the formation. Scale bar is 5 μm.

may reflect a number of processes. For instance, the observations could indeed result from i) preservation of primary Mg signal in the depositional calcite, ii) various amounts of Mg incorporated into calcite during recrystallization and cementation during diagenesis, or even, iii) analyzing a 2D plane in a 3D crystal.

Possible Preservation of Primary Mg Signal

Seawater Mg/Ca has fluctuated over geologic time and has been suggested to strongly influence chalk production (Stanley and Hardie 1998). The estimated low seawater Mg/Ca ($<$ 1 mol/mol) during the Late Cretaceous likely enabled coccolithophores to produce massive chalk deposits because certain species of coccolithophores were able to multiply at higher rates (Stanley et al. 2005). Atlantic coccoliths of the late Tertiary and Quaternary (with notably higher Mg/Ca $>$ 2 molar than in the Cretaceous) have been shown to have ≈ 7 mmol/mol Mg/Ca (Milliman

1974). Laboratory experiments have demonstrated that many species of coccolithophores incorporate less Mg in their skeletal elements as Mg concentrations shift toward those found in the Late Cretaceous (Stanley et al. 2005; Ries 2010). Three different modern coccolithophores were cultured in artificial seawater of varying Mg/Ca (Stanley et al. 2005). These experiments suggested that at seawater Mg/Ca = 1 mol/mol, coccolith Mg/Ca would be 10 to 51 mmol/mol. Hasiuk et al. (2016) reported three bulk Mg/Ca values from the Tor Formation (6.4, 7.2, and 7.3 mmol/mol; mean 6.9) measured via an ICP-MS. These bulk measurements represent the average geochemistry of hundreds of thousands of LMC microcrystals and therefore represent primary Mg/Ca and diagenetic Mg/Ca. While Mg/Ca data found in the Tor Formation samples analyzed in this study fall within the range reported by Stanley et al. (2005) and Hasiuk et al. (2016), it must be observed that the cultured coccoliths all behaved very differently from each other. One exhibited no change in test Mg/Ca as seawater Mg/Ca increased, the second increased test Mg/Ca exponentially,
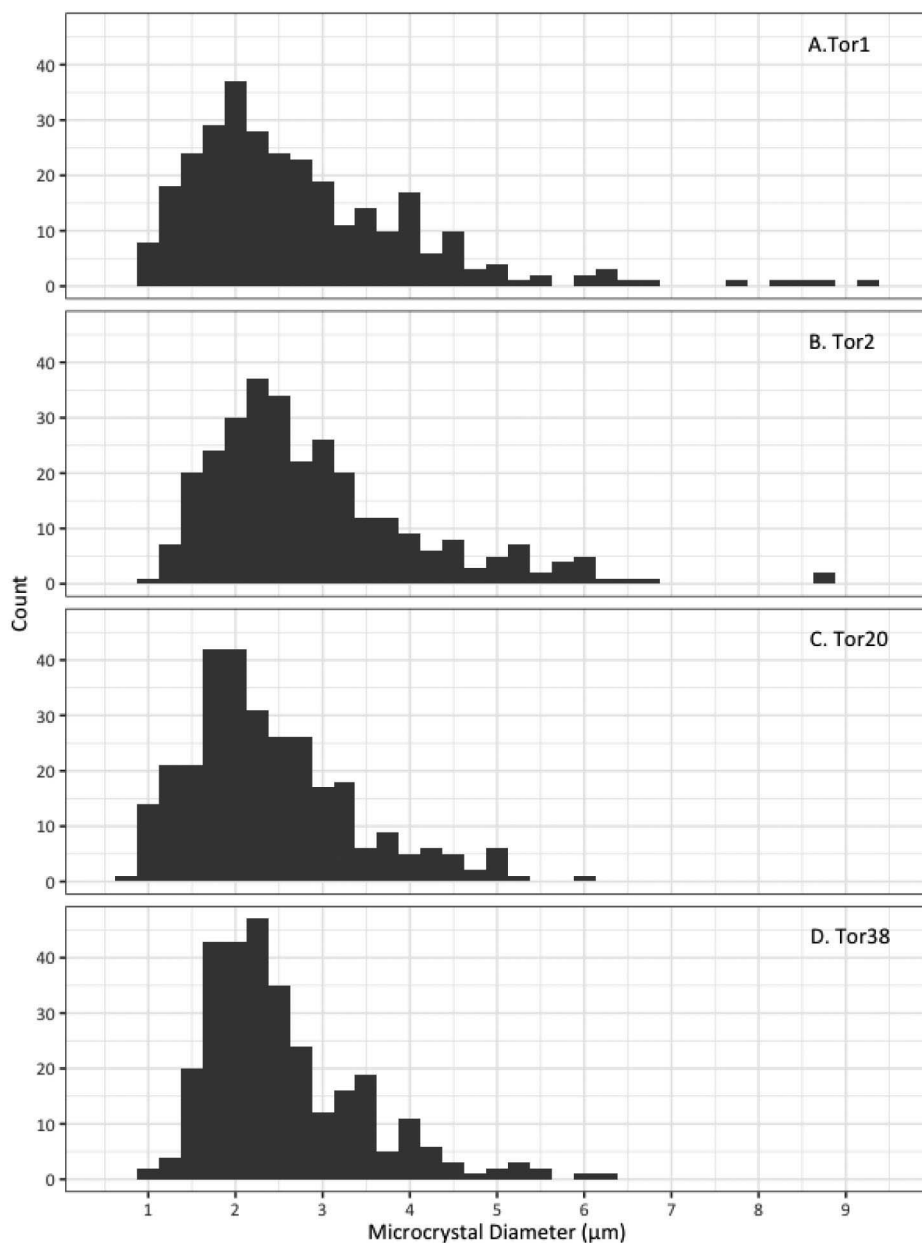
Fig. 5.—Crystal size distribution (CSD) of microcrystals from **A)** Tor1 (mean 2.7), **B)** Tor2 (mean 2.9), **C)** Tor20 (mean 2.4), and **D)** Tor38 (mean 2.6). Each histogram represents 300 microcrystals measured to the nearest 0.1 μm at 1500×. All four CSD define a positively skewed unimodal distributions with mean and median sizes noted.

and the third increased test Mg/Ca following a power law (Stanley et al. 2005; see review in Hasiuk and Lohmann 2010). These examples are different from other experimental data in calcifying organisms that show only power-law changes in test Mg/Ca with changes in seawater Mg/Ca. Furthermore, none of the cultured coccoliths in Stanley et al. (2005) produced the ≈ 7 mmol/mol Mg/Ca tests—the value observed in modern coccolith-rich sediments—when grown at modern seawater Mg/Ca (5.2 mol/mol).

Diagenetic Signal

While some depositional chemical signatures may be preserved, the low isotope values alone likely demonstrate diagenetic alteration during burial. The lack of a clear relationship between depth and $\delta^{18}O$ in the present data is likely an issue of sampling only a small interval (≈ 130 ft) in one well. The zonation-overgrowths found using SEM-EDS from this study are also strong evidence of a constructive diagenetic signal. A

recent laboratory LMC microcrystal precipitation study has challenged the *status quo* that microcrystal development occurs in the later stages of burial diagenesis and demonstrated that LMC microcrystals can develop early during the process of stabilization (Hashim and Kaczmarek 2020). Similar results can be found in a recent study which used clumped isotopes to demonstrate that 1–5 μm particles in a Maastrichtian chalk (Steven's quarry core from Danish Sector of the North Sea) are diagenetic calcite that formed in upper 100 m of burial, as a response to mineralogical stabilization of aragonitic components in the chalk (Tagliavento et al. 2020). With the onset of diagenesis in chalks occurring in the relatively early stages of burial, it is likely the zonation-overgrowths and heterogeneous calcite populations are recording primary chemistry, recrystallization, and cementation (Fig. 12) during different stages of diagenesis where parameters such as temperature, pressure, water chemistry, and water:rock ratio are dynamic.

In such a dynamic system, isolating a single variable which dictates LMC microcrystal texture may be difficult. However, Mg/Ca is well
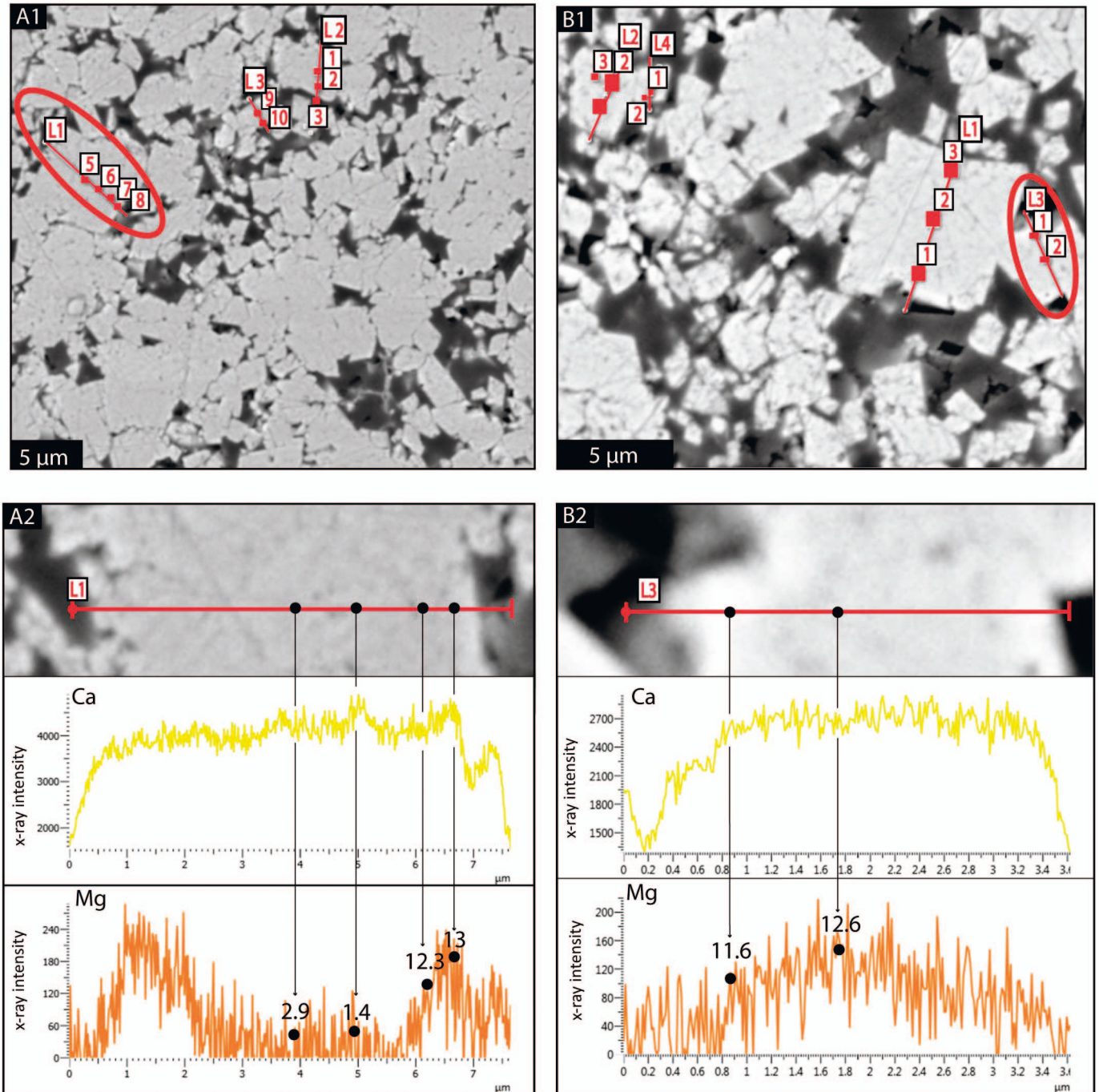
Fig. 6.—Line scans (solid red lines labeled L1, L2, etc.) and point analyses (labeled 1, 2, 3, etc.) from Tor1 sample. **A1)** SEM image of Area 2B taken from a polished surface and showing position of three-line scans and 10-point analyses. **A2)** Line scan of a large microcrystal ($\approx$ 7 μm), which shows distinct Mg/Ca zonation. The core of the microcrystal has low Mg/Ca (3 mmol/mol) and an elevated rim (12 mmol/mol). **B1)** SEM image of Area 3 showing four-line scans and 11-point analyses. **B2)** Smaller LMC microcrystal ($\approx$ 3 μm) has elevated Mg/Ca (12 mmol/mol). Line scans in A2 and B2 correspond to Ca (yellow) and Mg (orange) X-ray intensity versus distance along the line scan. Black dots represent point analyses and the corresponding Mg/Ca values at each point.

documented to be a crystal growth inhibitor and can significantly alter microcrystal morphology (Reeder 1996; Wasylenki et al. 2005). LMC microcrystal texture in the Tor Formation is predominantly granular-euhedral, so it is possible that the relatively low Mg/Ca did not "inhibit growth" and allow the formation of the euhedral LMC. A robust Mg/Ca data set obtained from SEM-EDS, which includes a wider range of textures found in microcrystalline limestones, may further give insight on the textural development of LMC in limestone.
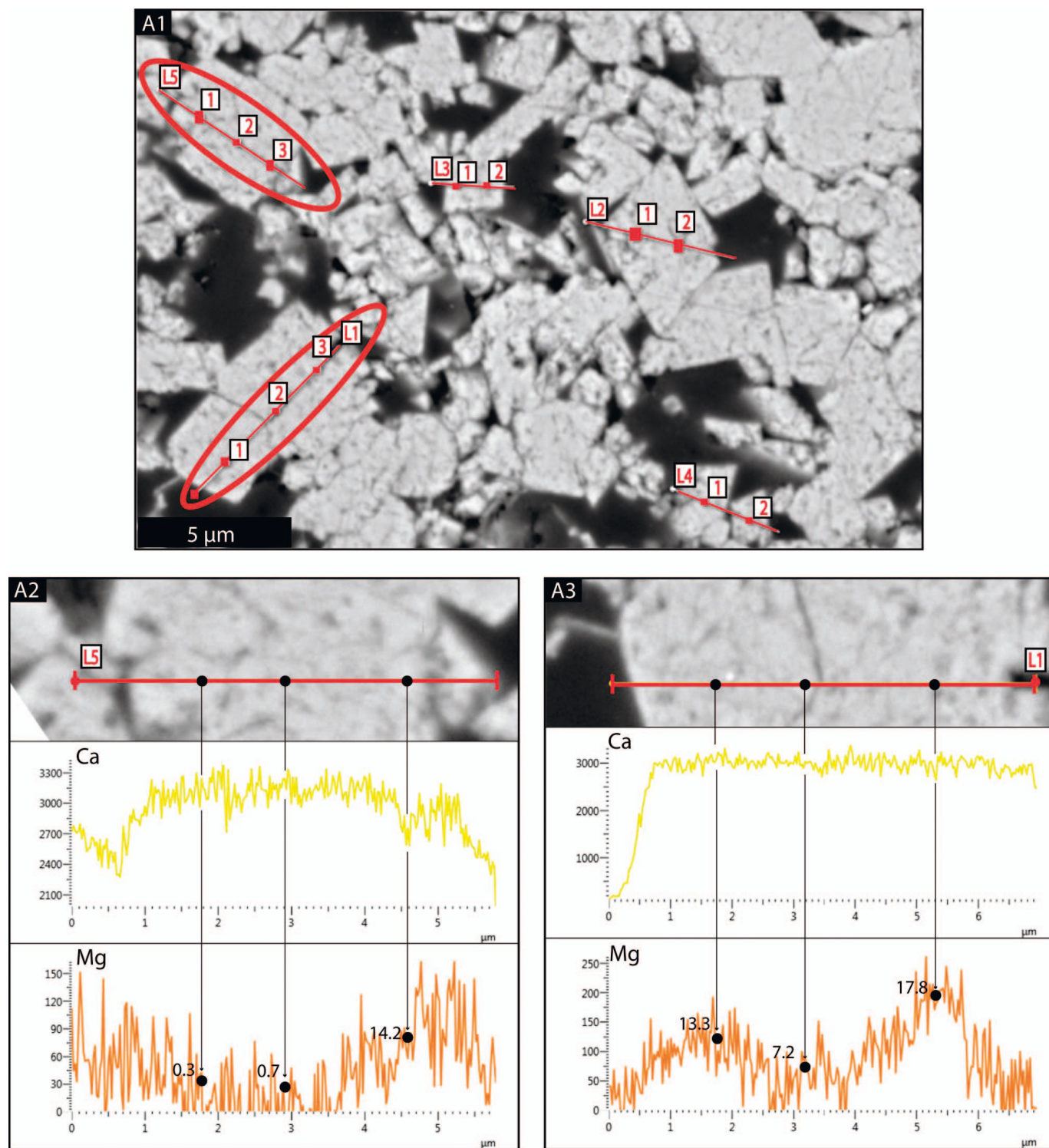
Fig. 7.—Line scans (solid red lines labeled L1, L2, etc.) and point analyses (labeled 1, 2, 3, etc.) from Tor2 sample. **A1)** SEM image of Area 2 taken from a polished surface and showing five-line scans and 12-point analyses. **A2)** Microcrystal ≈ 5 μm in diameter shows low Mg/Ca at the core (1 mmol/mol) and elevated Mg/Ca at the rim (14 mmol/mol). **A3)** Line scan of two separate microcrystals, each approximately 3 μm in diameter. The smaller microcrystal is elevated (13 mmol/mol) with respect to Mg. See Figure 6 caption for explanation of Ca and Mg X-ray intensity scans in A2 and A3.
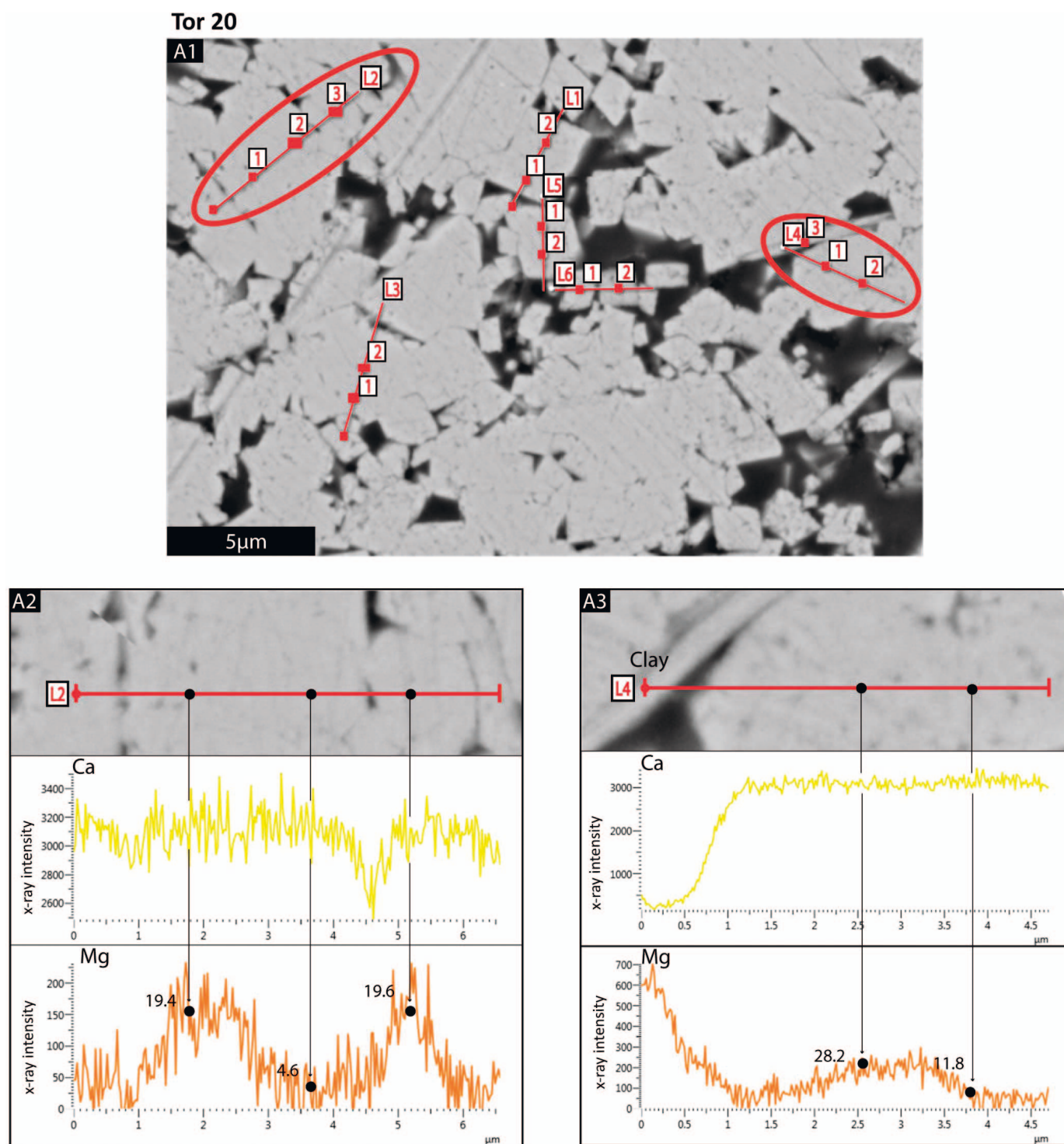
FIG. 8.—Line scans (solid red lines labeled L1, L2, etc.) and point analyses (labeled 1, 2, 3, etc.) from Tor20 sample. **A1)** SEM image of Area 2 taken from a polished surface showing six-line scans and 14-point analyses. **A2)** Line scan across two separate small microcrystals. The microcrystals show elevated Mg/Ca ratios ($\approx$ 19 mmol/mol). **A3)** Line scan across a clay grain and small LMC microcrystal. Clay grain shows high Mg/Ca, and LMC microcrystal has higher Mg/CA (28 mmol/mol). See Figure 6 caption for explanation of Ca and Mg X-ray intensity scans in A2 and A3.
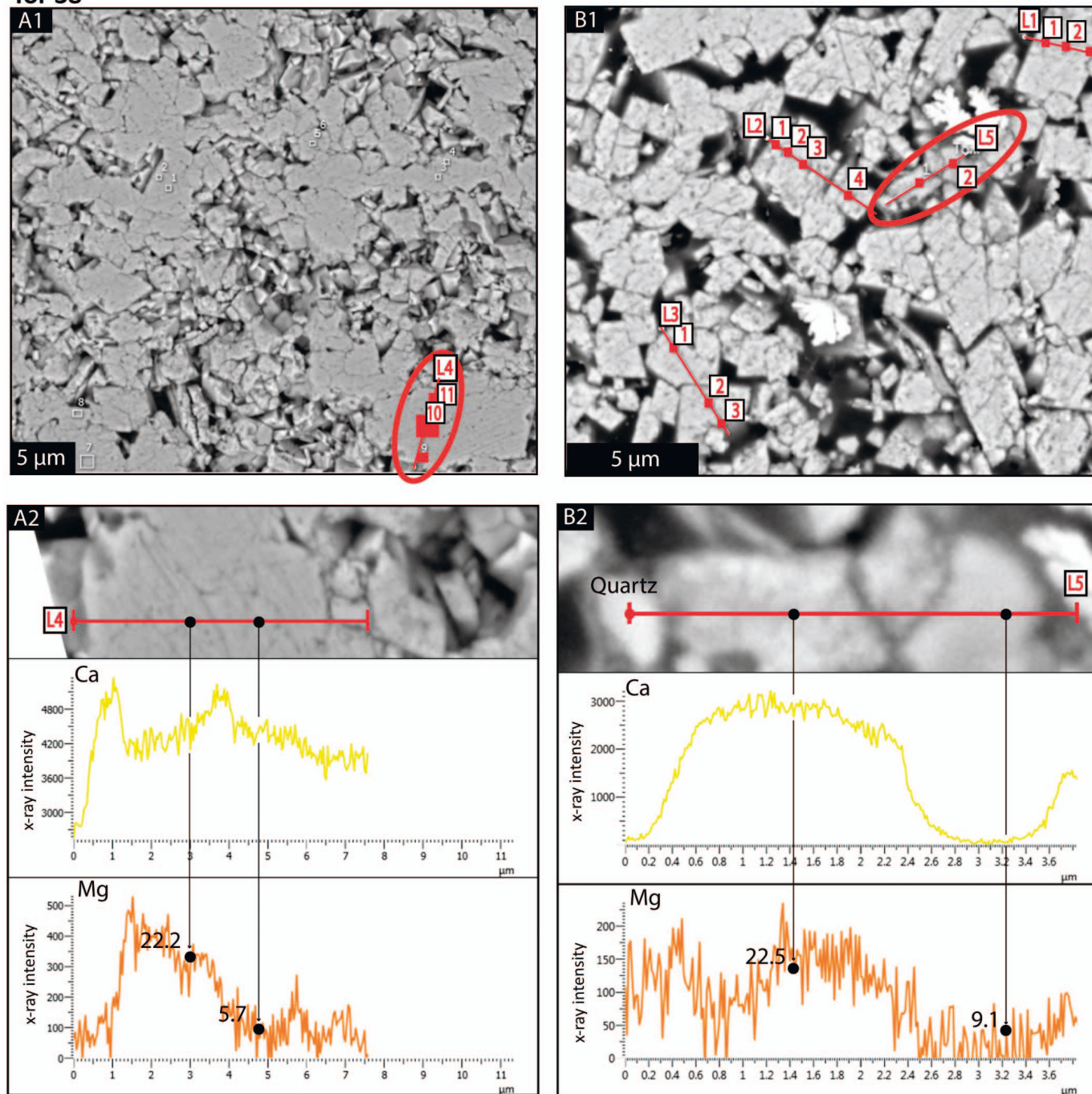
FIG. 9.—Line scans (solid red lines labeled L1, L2, etc.) and point analyses (labeled 1, 2, 3, etc.) from Tor38 sample. **A1)** SEM image from Area 1 taken from a polished surface and showing one line scan and three-point analyses. **A2)** Area 1, line scan 4 shows the quantitative line scan with quantitative point analysis. The crystal is approximately 7 μm in diameter and shows Mg/Ca zonation. **B1)** SEM image from Area 2 showing four-line scans and 11-point analyses. **B2)** Area 2 Line scan L5 from small microcrystal shows elevated Mg/Ca ratios. See Figure 6 caption for explanation of Ca and Mg X-ray intensity scans in A2 and B2.

2D vs. 3D Analysis

The process of creating a polished plug can create crystallographic artifacts. As there are a number of ways a crystal may be transected during polishing, the cross sections that we have analyzed—although chosen to be representative—may not yield a full-diameter cross section of the LMC microcrystal (Fig. 13). For example, it is possible that a large crystal is cut near the end of the crystal, giving the impression of a small microcrystal in a 2D cross section. In this case, what appears to be a small, chemically unzoned microcrystal, may actually be an artifact of analyzing only the rim of a larger microcrystal. Although microcrystals with well-defined crystal edges were selected for analysis, additional crystallographic techniques, such as electron-backscatter diffraction and orientation-imaging micros-

TABLE 1.—*LMC microcrystals analyzed by sample and area in each sample. Individual line scans are numbered with point analysis in each crystal also numbered. Asterisk represents large microcrystals. Each microcrystal Mg/Ca is represented, and each large microcrystal core and rim diameter is given.*

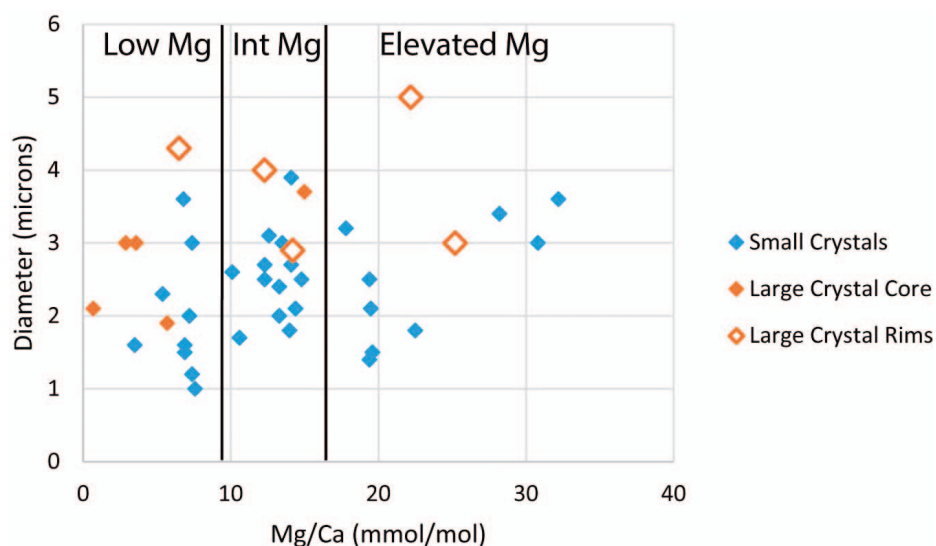| Sample	Area (n)	Line Scan (L)	Point Num.	Diameter (microns)			Mg/Ca (mmol/mol)	
				Microcrystal	Core	Rim	Core	Rim
Tor1	2b	1	5,6,7,8	7*	3.0	4.0	2.9	12.3
Tor1	2b	2	1,2	3.6	-	-	6.8	-
Tor1	2b	3	9,10	2.5	-	-	12.3	-
Tor1	2b	P	3,4	3.0	-	-	7.4	-
Tor1	3	1	1,2,3	8*	3.7	4.3	15.0	6.5
Tor1	3	2	1,2,3	3.6	-	-	32.2	-
Tor1	3	3	1,2	3.1	-	-	12.6	-
Tor1	3	4	1,2,3	1.4	-	-	19.4	-
Tor1	4	5	1,2	6*	3.0	3.0	3.6	25.2
Tor1	4	6	1,2	3.9	-	-	14.1	-
Tor1	4	7	1,2	2.0	-	-	7.2	-
Tor1	4	8	1,2	2.7	-	-	12.3	-
Tor1	4	9	1,2	1.2	-	-	7.4	-
Tor1	4	9	3	2.1	-	-	19.5	-
Tor2	2	1	1	2.4	-	-	13.3	-
Tor2	2	1	2,3	3.0	-	-	13.5	-
Tor2	2	2	1,2	3.2	-	-	17.8	-
Tor2	2	3	1,2	2.1	-	-	14.4	-
Tor2	2	4	1	1.8	-	-	14.0	-
Tor2	2	4	2	1.6	-	-	6.9	-
Tor2	2	5	1,2,3	5*	2.1	2.9	0.7	14.2
Tor20	2	1	1,2	2.9	-	-	14.3	-
Tor20	2	2	1,2	2.5	-	-	19.4	-
Tor20	2	2	3	1.5	-	-	19.6	-
Tor20	2	3	1,2	3.0	-	-	30.8	-
Tor20	2	4	1,2	3.4	-	-	28.2	-
Tor20	2	5	1,2	2.7	-	-	14.1	-
Tor20	2	6	1	1.0	-	-	7.6	-
Tor20	2	6	2	1.6	-	-	3.5	-
Tor38	1	4	9,10,11	6.9*	1.9	5.0	5.7	22.2
Tor38	2	1	1,2,3	2.6	-	-	10.1	-
Tor38	2	2	1,2,3	2.5	-	-	14.8	-
Tor38	2	2	4	1.5	-	-	6.9	-
Tor 38	2	3	1	2.3	-	-	5.4	-
Tor38	2	3	2,3	2.0	-	-	13.3	-
Tor38	2	4	1,2,3	1.7	-	-	10.6	-
Tor38	2	5	1	1.8	-	-	22.5	-

FIG. 10.—Graph showing the distribution of Mg/Ca values as a function of core/rim and large/small microcrystal groupings. The plots show three distinct phases of calcite from the Mg/Ca values. Four large cores and nine small microcrystals have the lowest Mg/Ca values (7.6 mmol/mol). The rims of three large microcrystals and 14 small microcrystals showed very similar intermediate Mg/Ca. The highest Mg/Ca values (17.8 mmol/mol) are found on the rims of two large microcrystals and nine small microcrystals.
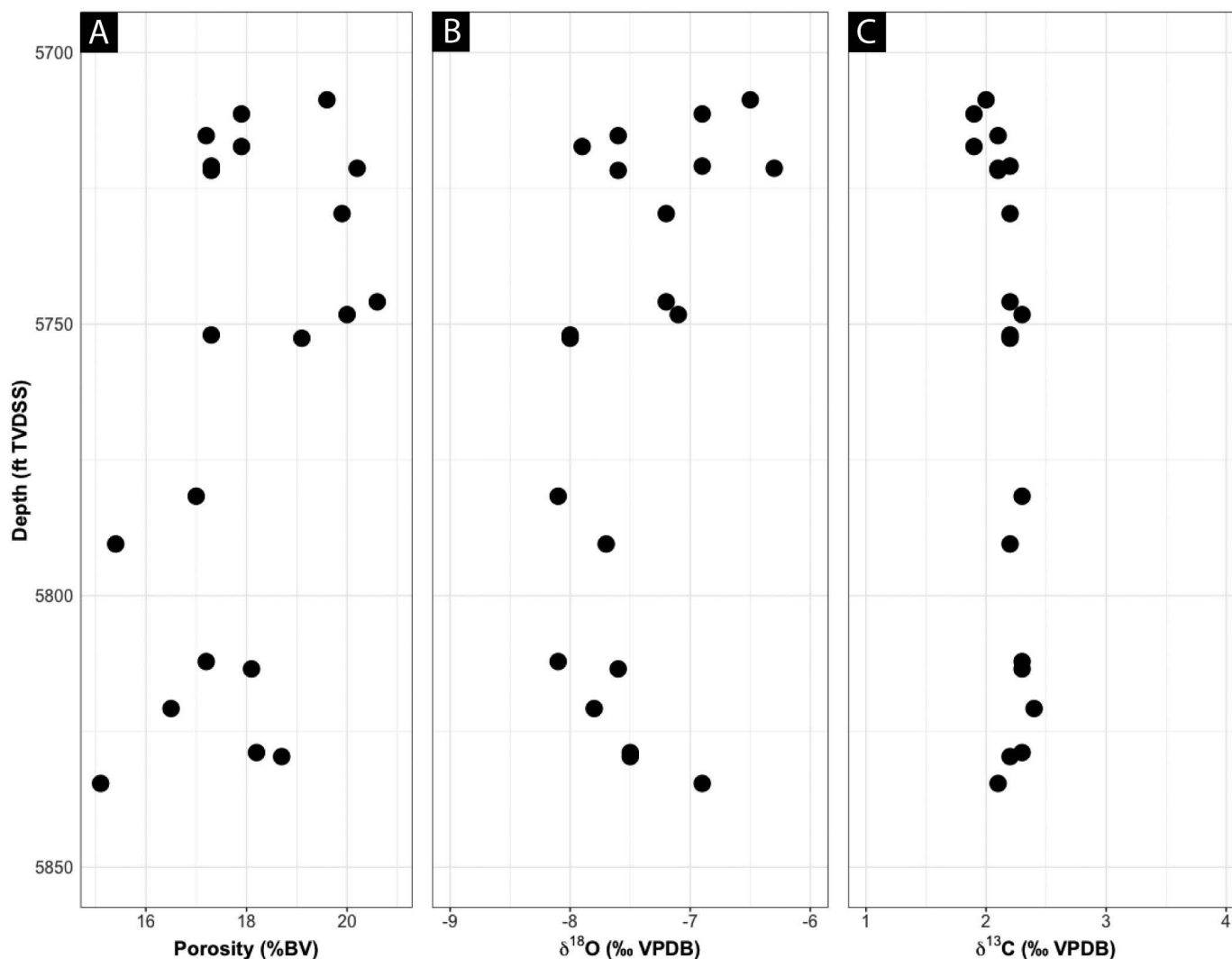
FIG. 11.—Helium porosity and stable-isotope data for the Tor Fm, plotted by depth. **A)** The interval has mean porosity of 18%, decreasing very little with depth, from an average of 18.8% in the uppermost 12 m to an average of 17.7% over the lowermost 13 m. **B)** $\delta^{18}O$ trends to lower values with increasing depth as samples 1–11 average –7.1‰ and samples 12–38 average –7.7‰ (VPDB). A correlation might be found with greater range in depth between samples. **C)** $\delta^{13}C$ shows little variation with depth (+1.9 to +2.4‰ VPDB $\delta^{13}C$).

copy (Dingley and Field 2013), would be required to more definitively evaluate the presence of such artifacts.

IMPLICATIONS FOR CHEMOSTRATIGRAPHY

Bulk-rock carbonate geochemistry (i.e., chemostratigraphy) has been used in chronostratigraphic correlations of ancient mixed carbonate–clastic successions and to assist in the assessment of how paleoenvironmental changes affect faunal turnover and biosedimentation (e.g., Jenkyns 1995; Davey and Jenkyns 1999; Wissler et al. 2003; Amodio et al. 2008; Huck et al. 2010, 2013; Vahrenkamp et al. 2010). Such chemostratigraphic studies are considered by some to hold large uncertainties because of what is perceived as unconstrained "wiggle matching" of isotopic trends (Christen and Litton 1995; Weissert et al. 2008), especially when used for chronostratigraphic correlations. There is no doubt that different isotope systems can be affected by localized processes, polymorph-specific isotope fractionation, and differing diagenetic histories (Immenhauser et al. 2002, 2003; Wendler 2013). However, it has become clearer through recent studies, in at least the case of $\delta^{13}C_{carbonate}$ bulk-rock analyses, that

comparison of multiple long-line datasets, each spanning hundreds of meters of strata, sampled at sufficient resolution (e.g., ≤ 25 cm), and coupled with biostratigraphic data, can, in fact, be correlated and used in the chronostratigraphic constraint of strata in individual basins and globally (cf. Oborny et al. 2020a, 2020b). Though robust for chronostratigraphic correlation, this methodology does not permit reliable analysis of primary isotopic signatures because of the potential remineralization of isotopically light $\delta^{13}C_{organic}$, which might overprint the true depositional chemistry in sampled carbonates. Therefore, studies aiming to calculate primary isotopic signatures (e.g., for the purpose of paleothermometry) must currently rely on direct sampling of shelly fauna, which in many cases are not prevalent.

It is often the practice to sample for $\delta^{13}C_{carbonate}$ from fine-grained matrix because of its LMC composition and supposed homogeneity (Immenhauser et al. 2003; Ludvigson et al. 2004; Panchuk et al. 2006; Saltzman 2002; Edwards and Saltzman 2016). However, bulk-sample analysis gives an average composition of hundreds of thousands of microcrystals that we have shown, at least in the case of the Tor Formation, to be a possible mixture of depositional and diagenetic LMC. Though
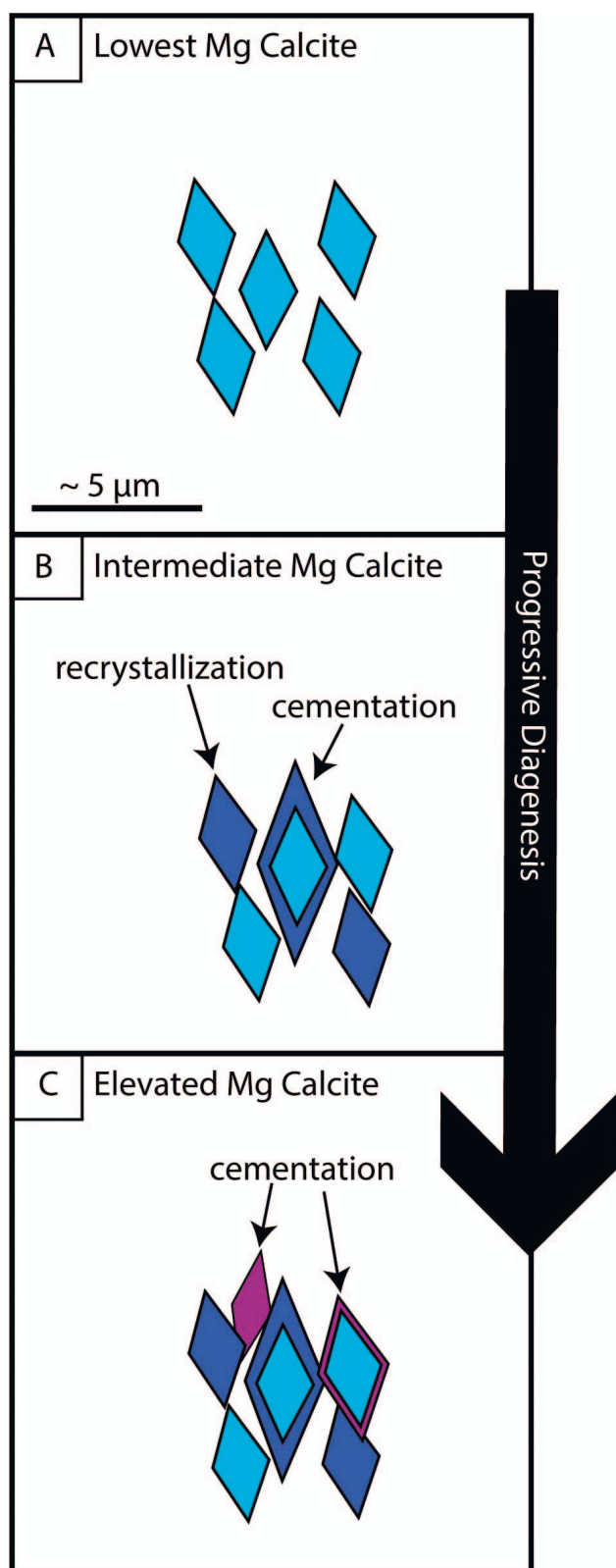
Fig. 12.—Precipitation model for LMC microcrystals. Lowest Mg; possible original disarticulated coccolith debris. Intermediate Mg added; recrystallization of some coccolith debris marked by intermediate Mg/Ca calcite phase, which also occurs as a cement on the rims of some larger crystals. Elevated Mg; rims of a Mg/Ca enriched phase of calcite is added as cement to some large crystals, and as individual small crystals that occlude pore space around existing recrystallized and non-recrystallized coccolith debris.

dissolution fabrics can be detected petrographically through recognition of dissolution "pits" or other cross cutting changes in morphologic features, precipitation fabrics can be difficult to visually identify—especially when a previous crystal morphology has been engulfed by a subsequent phase of crystal growth. This is why cathodoluminescence (Heydari and Moore 1993) and charge-contrast imaging (Griffin 2006) have been useful when studying macro-cements.

As demonstrated here, SEM-EDS can provide the chemistry of specific carbonate populations at the μm scale that may be more useful than bulk analyses when assessing diagenetic trends, estimating pore-fluid chemistry and/or pore-fluid evolution, or calculating paleo-temperatures. If primary sediment can be identified, isolated, and analyzed geochemically, perhaps with secondary-ion mass spectrometry (SIMS), results would yield a more accurate primary isotopic signature and improve paleoclimate interpretations. However, the resolution of SIMS is only now approaching the spot size capable of measuring within individual LMC microcrystals (Brodie et al. 2018).

CONCLUSION

The results of this study demonstrate that LMC microcrystals in a marine chalk can be heterogeneous in their Mg content (2.9 to 32.2 mmol/mol Mg/Ca) and that the largest crystals (≥ 5 μm) can be chemically zoned with respect to Mg. The Mg data suggests that some primary calcite may be preserved and demonstrates diagenetic phases can be distinguished chemically. Zonation and heterogeneity provide insight between microcrystals and the physiochemical processes by which those microcrystals develop. Distinct Mg/Ca (5.6 mmol/mol) was found in the cores of four larger LMC microcrystals (5–8 μm diameter) and in nine of the smaller microcrystals. The rims of the larger LMC microcrystals and the remainder of small microcrystals (< 5 μm diameter) reflect calcite in which the Mg/Ca is slightly elevated. The zonation and heterogeneity in LMC microcrystals may represent primary chemistry and various diagenetic signals.

Mg in the Tor Formation may not have inhibited crystal growth; LMC microcrystals have a granular-euhedral texture despite the documented variability in Mg. However, Mg has been shown to affect the morphology of calcite macrocrystals. Future work should focus on testing for zonation and diagenetic phases enriched with respect to Mg in the various textures of microcrystalline limestones—granular (subhedral or euhedral), clustered (loose or fused), and fitted (partial or fused)—to further improve our understanding of texture development as a function of Mg content.

Partitioning of Mg in LMC microcrystals suggests a closed geochemical system, and that recrystallization and calcite precipitation are occurring, but also that there is a distinct and measurable difference between the calcites in the Tor chalk. These distinctions may indicate that a primary geochemical fingerprint representative of primary depositional conditions may exist in chalk—and limestones more broadly—and potentially yield a reliable geochemical signal (e.g., $\delta^{18}O_{carbonate}$) that could be used for paleoenvironment and/or chemostratigraphic correlations.
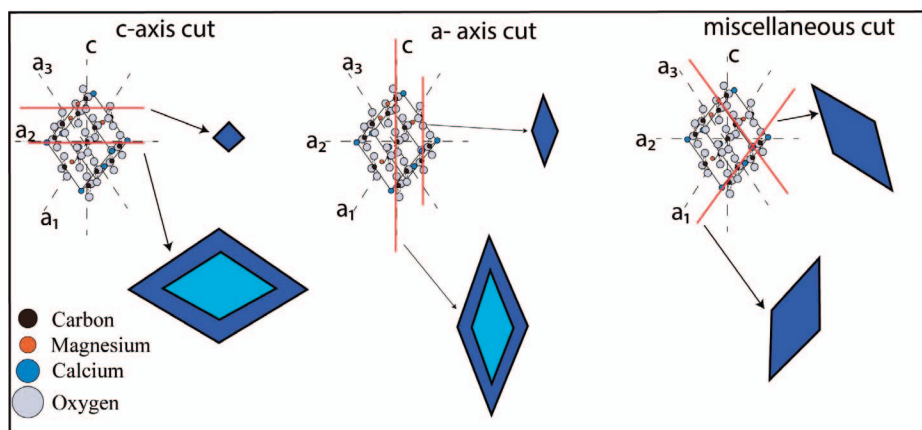
Fig. 13.—Possible LMC microcrystal 2D intersections. Each polished SEM image represents a 2D view of many 3D LMC microcrystals. The LMC microcrystal in view may not be a transect that divides the LMC microcrystal in two but rather could represent any number of off-plane transects through the microcrystal.

REFERENCES

AMERICAN PETROLEUM INSTITUTE, 1998, Recommended practices for core analysis: Recommended Practices, v. 40, p. 236.

AMODIO, S., FERRERI, V., D'ARGENIO, B., WEISSERT, H., AND SPROVIERI, M., 2008, Carbon-isotope stratigraphy and cyclostratigraphy of shallow-marine carbonates: the case of San Lorenzello, Lower Cretaceous of southern Italy: Cretaceous Research, v. 29, p. 803–813.

BACK, S., VAN GENT, H., REUNING, L., GRÖTSCH, J., NIEDERAU, J., AND KUKLA, P., 2011, 3D seismic geomorphology and sedimentology of the Chalk Group, southern Danish NorthSea: Geological Society of London, Journal, v. 168, p. 393–406.

BATHURST, R.G.C., 1975, Developments in Sedimentology 12, Carbonate Sediments and Their Diagenesis, Elsevier, 657 p.

BORRE, M., AND FABRICIUS, I.L., 1998, Chemical and mechanical processes during burial diagenesis of chalk: an interpretation based on specific surface data of deep-sea sediments: Sedimentology, v. 45, p. 755–769.

BOYLE, 1662, New Experiments Physico-Mechanical, Touching the Spring of the Air, and Its Effects: Oxford University Press.

BRODIE, M.W., APLIN, A.C., HART, B., ORLAND, I.J., VALLEY, J.W. AND BOYCE, A.J., 2018, Oxygen isotope microanalysis by secondary ion mass spectrometry suggests continuous 300-million-year history of calcite cementation and dolomitization in the Devonian Bakken Formation: Journal of Sedimentary Research, v. 88, p. 91–104.

BUDD, D., 1989, Micro-rhombic calcite and microporosity in limestones: a geochemical study of the Lower Cretaceous Thamama Group, UAE: Sedimentary Geology, v. 63, p. 293–311.

CANTRELL, D., AND HAGERTY, R., 1999, Microporosity in Arab Formation carbonates: GeoArabia, v. 4, p. 129–154.

CHRISTEN, J.A., AND LITTON, C.D., 1995, A Bayesian approach to wiggle matching: Journal of Archaeological Science, v. 22, p. 719–725.

COLLINS, C., ROWLANDS, N., STATHAM, P., AND HOLLAND, J., 2009, New large area silicon drift detectors: fast analysis without compromise: Microscopy Today, v. 17, p. 6–11.

DAVEY, S.D., AND JENKYNS, H.C., 1999, Carbon-isotope stratigraphy of shallow-water limestones and implications for the timing of Late Cretaceous sea-level rise and anoxic events (Cenomanian–Turonian of the peri-Adriatic carbonate platform, Croatia): Eclogae Geologicae Helvetiae, v. 92, p. 163–170.

DEVILLE DE PERIERE, M., DURLET, C., VENNIN, E., LAMBERT, L., BOURILLOT, R., CALINE, B., AND POLI, E., 2011, Morphometry of micrite particles in Cretaceous microporous limestones of the Middle East: influence on reservoir properties: Marine and Petroleum Geology, v. 28, p. 1727–1750.

DINGLY, D.J., AND FIELD, D.P., 2013, Electron Backscatter Diffraction and Orientation Imaging Microscopy: Materials Science and Technology, v. 13, p. 69–78.

DROUIN, D., COUTURE, A.R., JOLY, D., TASTET, X., AIMEZ, V., AND GAUVIN, R., 2007, CASINO V2.42: a fast and easy-to-use modeling tool for scanning electron microscopy and microanalysis users: scanning: Journal of Scanning Microscopies, v. 29, p. 92–101.

DUNN, W., 1975, North Sea basinal area, Europe: an important oil and gas province: Norges Geologiske Undersøkelse, v. 316, p. 69–97.

EDWARDS, C.T., AND SALTZMAN, M.R., 2016, Paired carbon isotopic analysis of Ordovician bulk carbonate ($\delta^{13}C_{carb}$) and organic matter ($\delta^{13}C_{org}$) spanning the Great Ordovician Biodiversification Event: Palaeogeography, Palaeoclimatology, Palaeoecology, v. 458, p. 102–117.

EKDALE, A.A., AND BROMLEY, R.G., 1984, Comparative ichnology of shelf-sea and deep-sea chalk: Journal of Paleontology, v. 58, p. 322–332.

FABRICIUS, I.L., 2003, How burial diagenesis of chalk sediments controls sonic velocity and porosity: American Association of Petroleum Geologists, Bulletin, v. 87, p. 1755–1778.

FABRICIUS, I.L., 2007, Chalk: composition, diagenesis and physical properties: Geologic Society of Denmark, Bulletin, v. 55, p. 97–128.

FOLK, R., 1965, Some aspects of recrystallization in ancient limestones, in Pray, L., and Murray, R., eds., Dolomitization and Limestone Diagenesis: SEPM, Special Publication 13, p. 14–48.

FRIEDMAN, G.M., 1964, Early diagenesis and lithification in carbonate sediments: Journal of Sedimentary Research, v. 34, p. 777–813

FULLMER, S.M., GUIDRY, S.A., GOURNAY, J., BOWLIN, E., OTTINGER, G., AL NEYADI, A., GUPTA, G., GAO, B., AND EDWARDS, E., 2014, Microporosity: characterization, distribution, and influence on oil recovery: International Petroleum Technology Conference, p. 1–17. doi:10.2523/IPTC-17629-MS

GOLDSTEIN, J.I., NEWBURY, D.E., ECHLIN, P., JOY, D.C., ROMIG, A.D., LYMAN, C.E., FIORI, C., AND LIFSHIN, E., 1992, Scanning Electron Microscopy and X-Ray Microanalysis: A Text for Biologists, Material Scientists, and Geologists: New York, Plenum Press, p. 417–523.

GOLDSTEIN, J.I., NEWBURY, D.E., MICHAEL, J.R., RITCHIE, N.W., SCOTT, J.H.J., AND JOY, D.C., 2017, Scanning Electron Microscopy and X-Ray Microanalysis: New York, Springer-Verlag, 539 p.

GRIFFIN, B.J., 2006, Charge contrast imaging of material growth and defects in environmental scanning electron microscopy: linking electron emission and cathodoluminescence: The Journal of Scanning Microscopies, v. 22, p. 234–242.

GRÜTZNER, J., AND MIENERT, J., 1999, Physical property changes as a monitor of pelagic carbonate diagenesis: an empirically derived diagenetic model for Atlantic Ocean basins: American Association of Petroleum Geologists, Bulletin, v. 83, p. 1485–1501.

HASHIM, M.S., AND KACZMAREK, S.E., 2019, A review of the nature and origin of limestone microporosity: Marine and Petroleum Geology, v. 107, p. 527–554.

HASHIM, M.S., AND KACZMAREK, S.E., 2020, Experimental stabilization of carbonate sediments to calcite: insights into the depositional and diagenetic controls on calcite microcrystal texture: Earth and Planetary Science Letters v. 538, n. 116235, p. 1–14.

HASHIM, M., AND KACZMAREK, S.E., 2021, Evolution of calcite microcrystal morphology during experimental dissolution: Journal of Sedimentary Research, v. 91, p. 229–242, doi:10.2110/jsr.2020.154.

HASIUK, F., AND LOHMANN, KC., 2010, Application of calcite Mg partitioning functions to the reconstruction of paleocean Mg/Ca: Geochimica et Cosmochimica Acta, v. 74, p. 6751–6763.

HASIUK, F., KACZMAREK, S., AND FULLMER, S., 2016, Diagenetic origins of the calcite microcrystals that host microporosity in limestone reservoirs: Journal of Sedimentary Research, v. 86, p. 1163–1178.

HEYDARI, E., AND MOORE, C.H., 1993, Zonation and geochemical patterns of burial calcite cements: Upper Smackover Formation, Clarke County, Mississippi: Journal of Sedimentary Petrology, v. 63, p. 44–60.

HUCK, S., RAMEIL, N., KORBAR, T., HEIMHOFER, U., WIECZOREK, T.D., AND IMMENHAUSER, A., 2010, Latitudinally different responses of Tethyan shoal-water carbonate systems to the Early Aptian oceanic anoxic event (OAE 1a): Sedimentology, v. 57, p. 1585–1614.

HUCK, S., HEIMHOFER, U., IMMENHAUSER, A., AND WEISSERT, H., 2013, Carbon-isotope stratigraphy of Early Cretaceous (Urgonian) shoal-water deposits: diachronous changes in carbonate-platform production in the north-western Tethys: Sedimentary Geology, v. 290, p. 157–174.

IMMENHAUSER, A., KENTER, J.A., GANSSEN, G., BAHAMONDE, J.R., VAN VLIET, A., AND SAHER, M.H., 2002, Origin and significance of isotope shifts in Pennsylvanian carbonates (Asturias, NW Spain): Journal of Sedimentary Research, v. 72, p. 82–94.

IMMENHAUSER, A., DELLA PORTA, G., KENTER, J.A., AND BAHAMONDE, J.R., 2003, An alternative model for positive shifts in shallow-marine carbonate $\delta^{13}C$ and $\delta^{18}O$: Sedimentology, v. 50, p. 953–959.

JAKOBSEN, F., AND ANDERSEN, C., 2010, Late Cretaceous basin development of the southern Danish Central Graben: Geological Survey of Denmark and Greenland, Bulletin, no. 20, p. 15–18.

JAMESON, J., 1994, Models of porosity formation and their impact on reservoir description, Lisburne field, Prudhoe Bay, Alaska: American Association of Petroleum Geologists, Bulletin, v. 78, p. 1651–1678.

JENKYNS, H.C., 1995, Carbon-isotope stratigraphy and paleoceanographic significance of the Lower Cretaceous shallow-water carbonates of Resolution Guyot, Mid-Pacific Mountains: Proceedings of the Ocean Drilling Program, Scientific Results, v. 143, p. 99–104.

JØRGENSEN, N.O., 1987, Oxygen and carbon isotope composition of Upper Cretaceous chalk from the Danish subbasin and the North Sea Central Graben: Sedimentology, v. 34, p. 559–570.

KACZMAREK, S.E., FULLMER, S.M., AND HASIUK, F.J., 2015, A universal classification scheme for the microcrystals that host limestone microporosity: Journal of Sedimentary Research, v. 85, p. 1197–1212.

LAKSHTANOV, L.Z, OKHRIMENKO, D.V., KARASEVA, O.N., AND STIPP, S.L.S., 2018, Limits on calcite and chalk recrystallization: Crystal Growth & Design, v. 18, p. 4536–4543.

LEVERETT, M., 1941, Capillary behavior in porous solids: Transactions of the American Institute of Mining and Metallurgical Engineers, v. 142, p. 152–169, doi:10.2118/941152-G.

LIND, I.L., 1993, Stylolites in chalk from Leg 130, Ontong Java Platteau, in Berger, W.H., Kroenke, L.W., and Mayer, L.A., eds., Proceedings of the Ocean Drilling Program, Scientific Results: College Station, Texas, v. 130, p. 445–451.

LOUCKS, R., LUCIA, F.J., AND WAITE, L., 2013, Origin and description of the micropore network within the lower Cretaceous Stuart City Trend tight-gas limestone reservoir in Pawnee Field in South Texas: Gulf Coast Association of Geological Societies, Journal, v. 2, p. 29–41.

LUCIA, F.J., 2007, Carbonate Reservoir Characterization: An Integrated Approach: Berlin, Springer, 336 p.

LUCIA, F.J., 2017, Observations on the origin of micrite crystals: Marine and Petroleum Geology, v. 86, p. 823–833.

LUCIA, F.J., AND LOUCKS, R.G., 2013, Micropores in carbonate mud: early development and petrophysics: Gulf Coast Association of Geological Societies, Journal, v. 2, p. 1–10.

LUDVIGSON, G.A., WITZKE, B.J., GONZÁLEZ, L.A., CARPENTER, S.J., SCHNEIDER, C.L., AND HASIUK, F., 2004, Late Ordovician (Turinian–Chatfieldian) carbon isotope excursions and their stratigraphic and paleoceanographic significance: Palaeogeography, Palaeoclimatology, Palaeoecology, v. 210, p. 187–214.

MALIVA, R., MISSIMER, T., CLAYTON, E., AND DICKSON, J., 2009, Diagenesis and porosity preservation in Eocene microporous limestones, South Florida, USA: Sedimentary Geology, v. 217, p. 85–94.

MEYERS, W.J., AND LOHMANN, KC., 1985, Isotope geochemistry of regionally extensive calcite cement zones and marine components in Mississippian limestones, New Mexico, in Schneiderman, N., and Harris, P.M., eds., Carbonate Cements: SEPM, Special Publication 36, p. 223–240.

MILLIMAN, J.D., 1974, Marine Carbonates, Part I: Berlin, Springer-Verlag, 375 p.

MØLLER, J.J., AND RASMUSSEN, E.S., 2003, Middle Jurassic–Early Cretaceous rifting of the Danish Central Graben. The Jurassic of Denmark and Greenland: Geological Survey of Denmark and Greenland, Bulletin, no. 1, p. 247–264.

MOSHIER, S., 1989, Development of microporosity in a micritic limestone reservoir, Lower Cretaceous, Middle East: Sedimentary Geology, v. 63, p. 217–240.

NIAZI, A.M.K., JAHREN, J., MAHMOOD, I., AND JAVAID, H., 2019, Reservoir quality in the Jurassic sandstone reservoirs located in the Central Graben, North Sea: Marine and Petroleum Geology, v. 102, p. 439–454.

OBORNY, S.C., CRAMER, B.D., AND BRETT, C.E., 2020a, High-Resolution Event Stratigraphy (HiRES) of the Silurian across the Cincinnati Arch (USA) through integrating conodont and carbon isotope biochemostratigraphy, with gamma-ray and sequence stratigraphy: Geologiska Föreningen, v. 142, p. 309–324, doi:10.1080/11035897.2020.1819407.

OBORNY, S.C., CRAMER, B.D., BRETT, C.E., AND BANCROFT, A.M., 2020b, Integrated Silurian conodont and carbonate carbon isotope ($\delta^{13}C_{carb}$) bio-chemostratigraphy of the East-Central Appalachian Basin: Palaeogeography, Palaeoclimatology, Palaeoecology, v. 554, p. 1–16.

OLDERSHAW, A.E., 1972, Microporosity control in microcrystalline carbonate rocks, southern Ontario, Canada: International Geological Congress, Stratigraphy and Sedimentology, Proceedings, v. 6, p. 198–207.

PANCHUK, K.M., HOLMDEN, C.E., AND LESLIE, S.A., 2006, Local controls on carbon cycling in the Ordovician midcontinent region of North America, with implications for carbon isotope secular curves: Journal of Sedimentary Research, v. 76, p. 200–211.

PITTMAN, E., 1971, Microporosity in carbonate rocks: American Association of Petroleum Geologists, Bulletin, v. 55, p. 1873–1878.

REEDER, R.J., 1996, Interaction of divalent cobalt, zinc, cadmium and barium with the calcite surface during layer growth: Geochimica et Cosmochimica Acta, v. 60, p. 1543–1552.

REZAEE, M.R., AND KAZEMZADEH, J.E., 2006, Relationships between permeability, porosity and pore throat size in carbonate rocks using regression analysis and neural networks: Journal of Geophysics and Engineering, v. 3, p. 370–376.

RIES, J.B., 2010, Review: geological and experimental evidence for secular variation in seawater Mg/Ca (calcite–aragonite seas) and its effects on marine biological calcification: Biogeosciences, v. 7, p. 2795–2849.

RYAN, B.H., KACZMAREK, S.E., AND RIVERS, J., 2019, Dolomite dissolution: an alternative pathway for the formation of palygorskite clay: Sedimentology, v. 66, p. 1803–1824, doi:10.1111/sed.12559.

SALTZMAN, M.R., 2002, Carbon isotope ($\delta^{13}C$) stratigraphy across the Silurian–Devonian transition in North America: evidence for a perturbation of the global carbon cycle: Palaeogeography, Palaeoclimatology, Palaeoecology, v. 187, p. 83–100.

SANDBERG, P.A., 1983, An oscillating trend in Phanerozoic non-skeletal carbonate mineralogy: Nature, v. 305, p. 19–22.

SCHLANGER, S.O., AND DOUGLAS, R.G., 1974, The Pelagic ooze–chalk–limestone transition and its implications for marine stratigraphy, in Hsü, K.J., and Jenkyns, H.C., eds., Pelagic Sediments: on Land and under the Sea: International Association of Sedimentologists, Special Publication 1, p. 117–148.

SCHOLLE, P., 1977, Chalk diagenesis and its relation to petroleum exploration: oil from chalks, a modern miracle?: American Association of Petroleum Geologists, Bulletin, v. 61, p. 982–1009.

SMIT, F.W.H., VAN BUCHEM, F.S.P., HOLST, J.C., LÜTHJE, M., ANDERSKOUV, K., THIBAULT, N., BUIJS, G.J.A., WELCH, M.J., AND STEMMERICK, L., 2018, Seismic geomorphology and origin of diagenetic geobodies in the Upper Cretaceous Chalk of the North Sea Basin (Danish Central Graben): Basin Research, v. 30, p. 895–925.

STANLEY, S.M., AND HARDIE, L.A., 1998, Secular oscillations in the carbonate mineralogy of reef-building and sediment-producing organisms driven by tectonically forced shifts in seawater chemistry: Palaeogeography, Palaeoclimatology, Palaeoecology, v. 144, p. 3–19.

STANLEY, S.M., RIES, J.B., AND HARDIE, L.A., 2005, Seawater chemistry, coccolithophore population growth, and the origin of Cretaceous chalk: Geology, v. 33, p. 593–596.

TAGLIAVENTO, M., JOHN, C.M., ANDERSKOUV, K., AND STEMMERIK, L., 2020, Toward a new understanding of the genesis of Chalk: diagenetic origin of micarbs confirmed by clumped isotope analysis: Sedimentology, v. 68, p. 513–530.

VAHRENKAMP, V.C., VAN BUCHEM, F.S.P., AND AL-HUSSEINI, M.I., 2010, Chemostratigraphy of the Lower Cretaceous Shu'aiba Formation: a $\delta^{13}C$ reference profile for the Aptian Stage from the southern Neo-Tethys Ocean, in Van Buchem, F.S.P., Al-Husseini, M.I., Maurer, F., and Droste, H.J., eds., Barremian–Aptian Stratigraphy and Hydrocarbon Habitat of the Eastern Arabian Plate: GeoArabia, Special Publication 4, p. 107–137.

VAN BUCHEM F., SMIT, F., BUIJS, G., TRUDGILL, B., AND LARSEN, P., 2018, Tectonostratigraphic framework and depositional history of the Cretaceous–Danian succession of the Danish Central Graben (North Sea): new light on a mature area: Geological Society of London, Petroleum Geology Conference Series. v. 8, p. 9–46.

VAN DEN BARK, E., AND THOMAS, O., 1981, Ekofisk: first of the giant oil fields in Western Europe: American Association of Petroleum Geologists, Bulletin, v. 65, p. 2341–2363.

VAN DER VOET, E., HEIJNEN, L., AND REIJMER, J., 2019, Geological evolution of the Chalk Group in the northern Dutch North Sea: inversion, sedimentation and redeposition: Geological Magazine, v. 156, p. 1265–1284.

VEJBÆK, O.V., AND ANDERSEN, C., 2002, Post mid-Cretaceous inversion tectonics in the Danish Central Graben: regionally synchronous tectonic events: Geological Society of Denmark, Bulletin, no. 49, p. 93–204.

VINCENT, B., FLEURY, M., SANTERRE, Y., AND BRIGAUD, B., 2011, NMR relaxation of neritic carbonates: an integrated petrophysical and petrographical approach: Journal of Applied Geophysics, v. 74, p. 38–58.

VOLERY, C., DAVAUD, E., DURLET, C., CLAVEL, B., CHAROLLAIS, J., AND CALINE, B., 2010a, Microporous and tight limestones in the Urgonian Formation (late Hauterivian to early Aptian) of the French Jura Mountains: focus on the factors controlling the formation of microporous facies: Sedimentary Geology, v. 230, p. 21–34.

VOLERY, C., DAVAUD, E., FOUBERT, A., AND CALINE, B., 2010b, Lacustrine microporous micrites of the Madrid Basin (late Miocene, Spain) as analogues for shallow-marine carbonates of the Mishrif Reservoir Formation (Cenomanian to early Turonian, Middle East): Facies, v. 56, p. 385–397.

WASYLENKI, L.E., DOVE, P.M., AND DE YOREO, J.J., 2005, Effects of temperature and transport conditions on calcite growth in the presence of Mg^{2+}: implications for paleothermometry: Geochimica et Cosmochimica Acta, v. 69, p. 4227–4236.

WEISSERT, H., JOACHIMSKI, M., AND SARNTHEIN, M., 2008, Chemostratigraphy: Newsletters on Stratigraphy, v. 42, p. 145–179.

WENDLER, I., 2013, A critical evaluation of carbon isotope stratigraphy and biostratigraphic implications for Late Cretaceous global correlation: Earth-Science Reviews, v. 126, p. 116–146.

WISSLER, L., FUNK, H., AND WEISSERT, H., 2003, Response of Early Cretaceous carbonate platforms to changes in atmospheric carbon dioxide levels: Palaeogeography, Palaeoclimatology, Palaeoecology, v. 200, p. 187–205.